Available online at www.sciencedirect.com
ScienceDirect
Coordination Chemistry Reviews 251 (2007) 1101–1127
COORDINATION CHEMISTRY REVIEWS
www.elsevier.com/locate/ccr

Review

# Time resolved thermodynamics of ligand binding to heme proteins

Randy W. Larsen [a,*], Jaroslava Mikšovská [b]

[a] *Department of Chemistry, University of South Florida, 4202 E. Fowler Ave. SCA 400, Tampa, FL 33620, USA*
[b] *Department of Chemistry, Marshall University, One John Marshall Drive, Huntington, WV 25755, USA*

Received 30 April 2006; accepted 25 August 2006
Available online 30 August 2006

## Contents



## Abstract

Understanding the thermodynamics of ligand binding in metallo-proteins is of critical importance in probing the underlying energetic basis for the reaction mechanism. However, many kinetic events occurring subsequent to ligand binding/release are on a time scale outside of that accessible using traditional calorimetric techniques thus making the construction of thermodynamic profiles for early kinetic events difficult. Photothermal methods have enjoyed considerable success in probing photo-triggered reactions on timescales ranging from ∼ns to >ms. These techniques, including photoacoustic calorimetry (PAC) and photothermal beam deflection (PBD), have been applied to obtain both molar volume and enthalpy

*Abbreviations:* 2-MeIm, 2-methylimidazole; *Bj*FixL, *Bradorhizobium japonicum* FixL; Cbo, cytochrome $bo_3$ from *E. coli*; CcO, cytochrome *c* oxidase from bovine heart; CD/MCD, circular dichroism/magnetic circular dichroism; COMVCcO, CO-mixed valence cytochrome *c* oxidase; CTAB, cetylmethylammonium bromide; ET, electron transfer; EPR, electron paramagnetic resonance; EXAFS, extended X-ray absorption fine structure; Fe(II)4SP, $Fe^{II}$ *meso*-tetrakis(4-sulphonatophenyl)-porphyrin; FeIIPPIX, Fe(II) protoporphyrin IX; FTIR, Fourier transform infra-red; HbA, human hemoglobin A; hhMB, horse heart myoglobin; HOMO/LUMO, highest occupied molecular orbital/lowest unoccupied molecular orbital; Mb, myoglobin; MP-11, microperoxidase-11; PAC, photoacoustic calorimetry; PBD, photothermal beam deflection; RbCcO, *Rb. sphaeroides* cytochrome *c* oxidase; *Sm*FixL, *Sinorhizobium meliloti* FixL; swSMb, sperm whale myoglobin

* Corresponding author. Tel.: +1 813 974 7925.
*E-mail address:* rlarsen@cas.usf.edu (R.W. Larsen).

0010-8545/$ – see front matter © 2006 Elsevier B.V. All rights reserved.
doi:10.1016/j.ccr.2006.08.018

changes for a wide range of biological processes including ligand binding to metallo-proteins. Here we review the progress made to date in utilizing photothermal methods (PAC and PBD) to probe the thermodynamics of small molecule binding to heme proteins ranging from simple globin-type proteins to the more complex heme/copper oxidases.
© 2006 Elsevier B.V. All rights reserved.

*Keywords:* Photothermal methods; Photoacoustic calorimetry; Photothermal beam deflection; Heme; FixL; Cytochrome *c* oxidase; Myoglobin; Transient spectroscopy

## 1. Introduction

### 1.1. Iron porphyrins

Metallo-porphyrins represent a diverse class of coordination complexes that can perform an extraordinary array of complex catalytic reactions depending upon the nature of the central metal. The catalytic activity of these molecules depends, to a large extent, on the electronic structure of the porphyrin macrocycle and the spin/coordination state of the central metal. In the absence of a metal the porphyrin ring adopts a $D_{2h}$ symmetry that is responsible for two dominant optical transitions in the near UV–vis region of the optical spectra (Figs. 1 and 2). The four molecular orbitals that are involved in the prominent optical transitions are the highest occupied molecular orbital (HOMO) ($a_u$ symmetry), the HOMO-1 ($b_{3u}$ symmetry), LUMO ($b_{2g}$ symmetry) and the LUMO + 1 ($b_{1g}$ symmetry) [1–3]. This gives rise to a $1^1A_g$ ground state and $1^1B_{1u}$, $1^1B_{2u}$, $2^1B_{1u}$, and $2^1B_{2u}$ excited states with oscillator strengths 0.02, 0.07, and 1.15 (sum of the oscillator strengths for the $2^1B_{1u} \leq 1^1A_g$ and $2^1B_{2u} \leq 1^1A_g$ transitions) [4]. The high oscillator strength transitions give rise to the B-band (more commonly referred to as the Soret transition). The difference in oscillator strength between the Q and B bands arises from the addition of the transition dipoles between one electron states in the B-band and a near cancellation of the one electron dipoles in the Q-band due to strong configuration interaction.

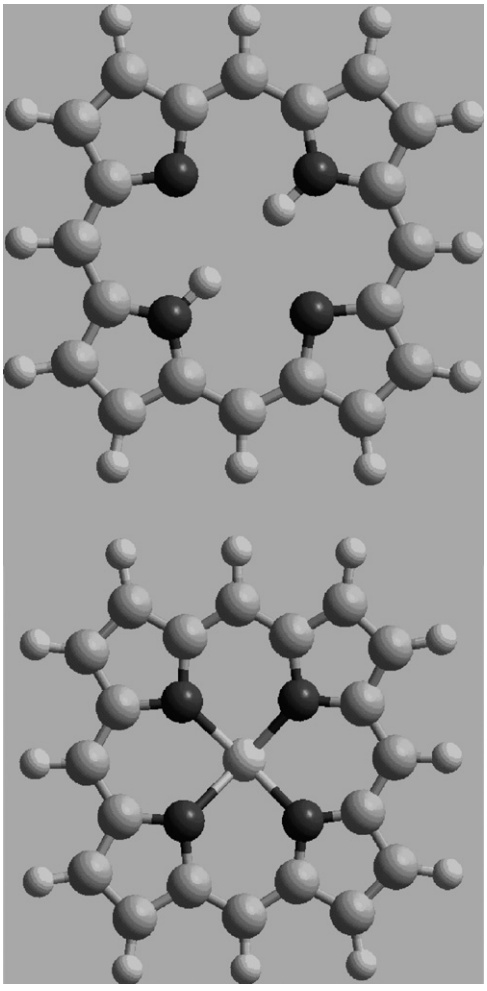

Fig. 1. Structural diagram of both free-base and metallo-porphyrin illustrating the difference in porphyrin symmetry.

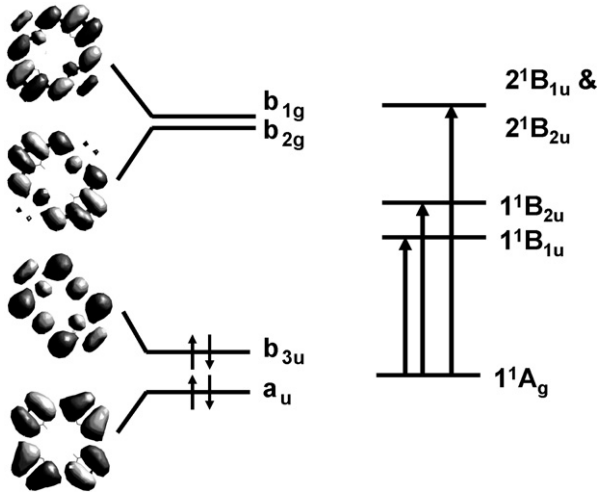


Fig. 2. Molecular orbital diagram (left) and molecular states for free-base porphyrin with $D_{2h}$ symmetry.

Metalloporphyrins essentially raise the symmetry of the porphyrin from $D_{2h}$ to $D_{4h}$ but the salient features of the absorption spectra are retained between the free-base and metallated forms of the macrocycle. Under $D_{4h}$ symmetry the lowest occupied MOs of the porphyrin are of $a_{1u}$ and $a_{2u}$ symmetry with a degenerate set of orbitals with $e_g$ symmetry make up the LUMO. The porphyrin optical spectrum for these systems is best described using a four orbital model originally proposed by Gouterman that involves extensive configuration between the nearly degenerate $a_{2u}$ and $a_{1u}$ HOMO orbitals and the degenerate set of $e_g^*$ LUMO orbitals (see Fig. 3) [5,6]. The ground state of the $D_{4h}$ porphyrin π-system has an electron configuration $\ldots(a_{2u})^2(a_{1u})^2$ producing an $^1A_{1g}$ state. The excited electron configurations $\ldots(a_{2u})^2(a_{1u})^1(e_{gx})^1$, $\ldots(a_{2u})^2(a_{1u})^1(e_{gy})^1$, $\ldots(a_{2u})^1(a_{1u})^2(e_{gy})^1$, and $\ldots(a_{2u})^1(a_{1u})^2(e_{gx})^1$. These configurations interact via the two electron repulsion term $\boldsymbol{H}' = e'^2/r_{ij}$ giving rise to the energy level diagram shown in Fig. 3 where $A'_{1g}$ is the average energy splitting of the $a_{2u}$ and $a_{1u}$ orbitals and $A''_{1g}$

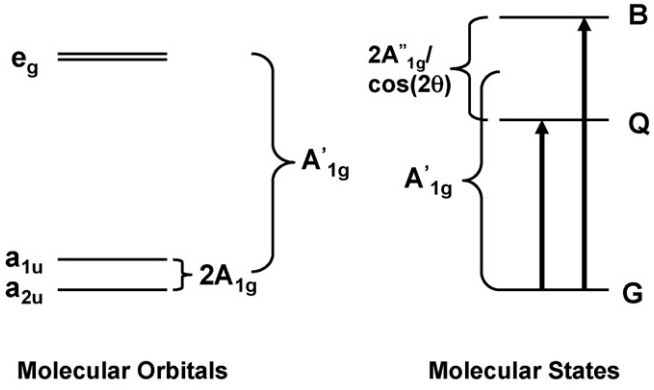


Fig. 3. Diagram showing the four orbital model used to describe the optical spectrum of metallo-porphyrins with $D_{4h}$ symmetry.

is the matrix element that couples the excited electron configurations (e.g., $\langle(a_{2u}e_{gx})|\boldsymbol{H}|(a_{2u}e_{gx})\rangle$). Transitions between these states give rise to the B and Q band transitions and accurately reflects the difference in molar extinction coefficient.

Introduction of a transition metal atom to the porphyrin core results in shifts in the relative energies of the $a_{2u}/a_{1u}$ orbital energies thus effecting the $A'_{1g}$ matrix element and the B and Q band positions [1–3,6]. In addition, the 3d orbitals of the metal can also interact directly with porphyrin molecular orbitals of the same symmetry. Since the metal orbitals transform as $b_{1g}$ ($3d_{x^2-y^2}$), $a_{1g}$ ($3d_{z^2}$), $b_{2g}$ ($3d_{xy}$), $e_g$ ($3d_{xz}$, $3d_{yz}$) in $D_{4h}$, only the $e_g$ ($3d_{xz}$, $3d_{yz}$) orbitals can mix with the porphyrin $e_g^*$ (π-orbitals) (see Fig. 4). Occupancy of the metal $3d_{xz}$ and $3d_{yz}$ orbitals can then influence the electronic properties of the metalloporphyrin.

The catalytic versatility of iron-porphyrins has been exploited by nature to perform a wide variety of chemical processes. This versatility is due to: (1) the broad range of reduction potentials of the central iron that can be readily modulated by axial ligands, (2) vacant d-orbitals on the central iron atom that can mediate a wide range of metal–ligand–porphyrin ring interactions essential for catalytic enhancement, (3) the ability to form coordinatively stable interactions between protein donated amino acids (e.g., His, Cys, etc.) and the heme iron, and (4) the ability of the heme iron to back donate electron density into anti-bonding orbitals on small gaseous ligands such as CO and $O_2$.

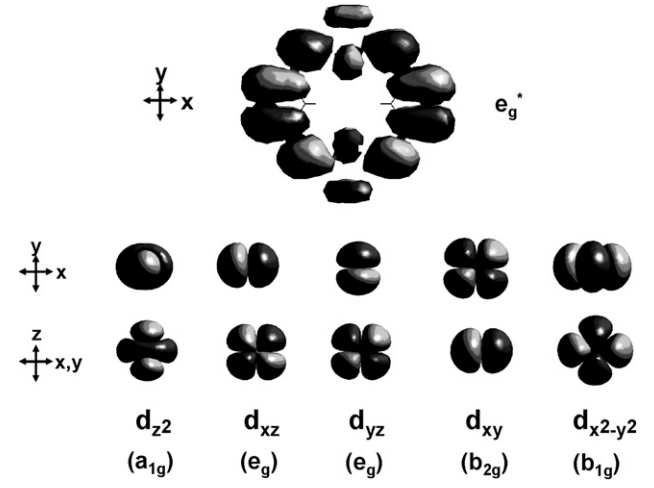


Fig. 4. Molecular orbital diagram for the porphyrin π-system (top) and transition metal atomic orbitals (bottom).

### 1.2. Heme proteins: structure and function

Heme proteins are one of the most widely distributed metalloprotein in nature [7–10]. Heme proteins participate in electron transfer (cytochromes), oxygenation (mono-oxygenases), hydrogen peroxide degradation (peroxidases, catalases), small molecule sensing (FixL, PAS domain sensors, and HemAT sensors), transcription regulation (CooA type proteins), energy transduction (heme/copper oxidases, cytochrome $bc_1$, etc.), oxygen transport and storage (hemoglobins and myoglobins) and polymer synthesis/degradation (lignan peroxidase, etc.). Heme proteins contain an iron protoporphyrin IX active site (or a derivative of this macrocycle) and are coordinated to the protein via amino acids containing lone pairs of electrons such as histidine, methionine, tyrosine or cystein (some π-type interactions may be involved in histidine coordination). The structures of the various hemes found in nature are shown in Fig. 5.

The versatility of the heme group is exploited through the structural nature of the protein matrix. The nature of the proximal heme ligand can influence the degree of electron back donation into π-accepting ligands (in the six-coordination site), while residues making up the distal heme pocket strongly influence the orientation of bound ligands in the sixth coordination site as well as the lability of ligands such as dioxygen through H-bond interactions, hydrophobicity, etc. Distal heme pocket residues may also serve as substrate binding sites for proteins such as plant peroxidases and cytochrome $P_{450}$ and are designed to place the substrate in a specific orientation and at a specific distance from the heme active site to facilitate rapid and stereo-specific chemistry. The protein tertiary structure also provides conduits for ligand access to and from the heme active site. These ligand channels provide ready access from the solvent to the distal heme pocket and can be modulated by conformational changes resulting in 'gated' ligand access.

To fully understand the complexity through which heme proteins perform their physiological function as well as the subtle structural nuances that ultimately determine the specific chemistry performed by these proteins requires complete kinetic, structural and thermodynamic profiles for the physiological process under conditions as close to physiological as experimentally possible. To date a plethora of physical methods have been utilized to probe heme proteins with the most widely utilized being optical (including optical absorption, circular dichroism (CD) and magnetic circular dichroism (MCD) [11]), vibrational (including FTIR and resonance Raman [12,13] and magnetic spectroscopies (most notably EPR [14]). A vast majority of the kinetic and thermodynamic information available for ligand binding process in heme proteins has been obtained primarily from optical studies.

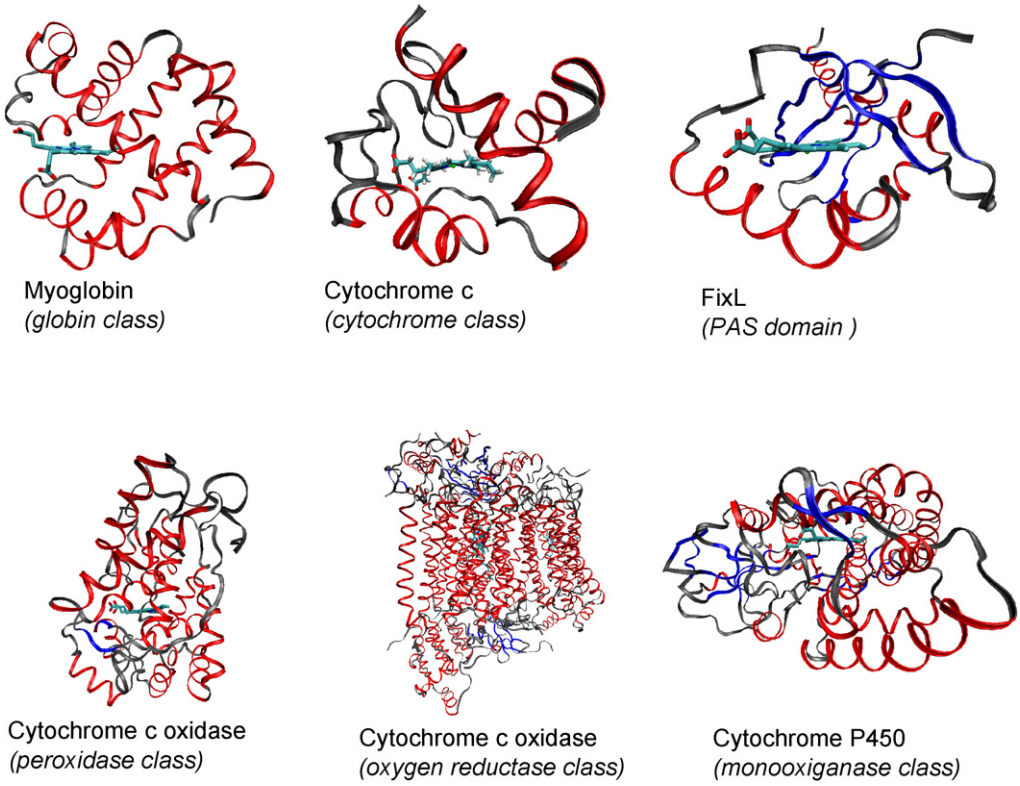


Fig. 5. Ribbon presentation of the structures of several classes of heme proteins. α-Helices are shown in red, β-sheets in blue and turn and random coil elements in gray.

### *1.3. Optical methods to study heme proteins*

By far the most widely used method for structure/function studies of heme proteins has been optical absorption spectroscopy. Equilibrium optical absorption is routinely utilized to determine the oxidation state and/or the nature of the axial ligation in heme proteins and is especially useful in determining these properties in newly discovered heme proteins (such as FixL and the HemAT class) as well as in heme protein mutants. Of greater utility is the use of time resolved optical spectroscopy to probe heme protein kinetics under more physiological conditions (see reference [15] for a recent review). In this type of experiment a perturbation is made to the protein (photolysis of a ligand, photoinjection of an electron, rapid solution heating, rapid pH jump, etc.) and the subsequent relaxation of the protein is monitored by following the changes in the heme spectra as a function of time. A classic example of this type of experiment is the photolysis of CO from CO bound human hemoglobin (HbA) [15–18]. Deoxy HbA exhibits a Soret maximum at 430 nm while that of the COHbA is found at 415 nm. Early studies monitoring the changes in absorbance as a function of time after full photolysis of CO bound HbA revealed five kinetics steps of ∼40 ns (geminate recombination), ∼1 μs (tertiary structural change), ∼20 μs (quaternary structural changes associated with the transition between high affinity (R) state and low affinity (T) state), ∼200 μs (quaternary structural transition together with CO binding) and ∼4 ms (CO recombination to the T-like quaternary structure). Further monitoring of the isosbestic point between the equilibrium deoxy and CO bound spectra as a function of time subsequent to photolysis has allowed for the kinetic complexity of the R–T transition to begin to be understood. In a similar way the photolysis of CO bound myoglobin (COMb) has revealed only two phases of CO recombination; a geminate recombination phase ($k_{gem} = 3 \times 10^8\ s^{-1}$) and a diffusion controlled rebinding phase ($k_1 = 7.6 \times 10^5\ M^{-1}\ s^{-1}$). Photolysis experiments on a large number of Mb mutants have now provided important details on the structural subtleties of the distal heme pocket in modulating ligand affinities [19].

Kinetic ligand binding studies have proved enormously successful in probing structure/function relationships in heme proteins. Fast kinetics studies have also been extremely useful in probing other reactions, such as electron transfer. For example, these studies have begun to illuminate the complex mechanism of dioxygen reduction and active proton transport in heme/copper oxidases found in nearly all aerobic organisms. In higher organisms these enzymes contain two heme chromophores and at least one copper ion (see later sections for a more detailed description of this class of enzymes). One heme and one copper ion together constitute a dioxygen reduction site while the remaining heme (and Cu ion in heme/copper oxidases from higher organisms) catalyze electron transfer from the substrate to dioxygen bound at the heme/copper binuclear center. One of the most successful strategies for probing the pathways of electron transfer as well as the kinetics/dynamics of the dioxygen chemistry has been to use the so called flow-flash method coupled with absorption spectroscopy [20,21]. In this experiment the enzyme is reduced with four electrons (in the bovine case) and CO is bound to the dioxygen reduction site. Under

these conditions dioxygen binds to the binuclear center with a rate constant equal to that of the CO dissociation rate from the heme ($0.03\,s^{-1}$) [22]. The fully reduced CO bound form of the enzyme is then rapidly mixed with oxygen saturated buffer and exposed to a short laser pulse which photodissociates the CO on a femtosecond time scale. The subsequent oxygen binding and intramolecular electron transfer within the enzyme is then monitored by probing changes in the heme optical absorption spectra. These studies have shown that the initial two electron reduction of dioxygen (formation of the so-called P-intermediate) occurs with a rate constant of roughly $3 \times 10^4\,s^{-1}$ which is followed by proton uptake with a rate constant of $\sim 1 \times 10^4\,s^{-1}$ [23–25]. Further electron transfer forming an oxyferryl species at the heme of the binuclear center occurs with a rate constant of $\sim 5 \times 10^3\,s^{-1}$. The fourth electron is then transferred with a rate constant of $\sim 500\,s^{-1}$. The use of enzyme reconstituted into phospholipid vesicles together with pH sensitive dyes has further allowed for the kinetics of active proton transport to be determined [24].

The above are just two examples of the utility of optical spectroscopy in unraveling kinetic complexity in heme containing proteins and enzymes. By coupling these methods together with site directed mutagenesis a more detailed picture of structure/function relationships in these proteins can be obtained.

### 1.4. Activation parameters and thermodynamics of ligand binding

Although the use of optical spectroscopy has been primarily focused upon unraveling the often complex kinetics involved with heme protein chemistry, similar methods can also be employed to obtain important information concerning the thermodynamics associated with heme protein reactions. Probing the thermodynamics of metalloprotein function is a critical component in understanding structure/function relationships. In the case of heme proteins, ligand binding, electron transfer, etc. provide at least part of the free energy required for catalysis and/or relevant conformational changes.

Ideally, in order to have a firm understanding of the reaction pathway in heme proteins a complete thermodynamic profile is required. Such a profile would map the magnitudes and time scales of thermodynamic changes (including enthalpy, volume, and entropy changes). There are a number of methods available for determining reaction enthalpy and entropy changes but these are typically equilibrium techniques (such as equilibrium binding titrations as a function of temperature (reaction enthalpies/entropies) and pressure (reaction volumes)). Reaction kinetics can also reveal information concerning the thermodynamic profiles. Knowledge of the thermodynamic properties of transition states between various intermediates within an enzymatic or ligand binding cycle can be utilized to construct the appropriate thermodynamic profile. This can be accomplished by monitoring the various reaction rates as a function of temperature or pressure and then fitting the data to the following expressions:

$$\ln\left(\frac{k_{obs}h}{k_bT}\right) = \frac{-\Delta H^{\ddagger}}{RT} + \frac{\Delta S^{\ddagger}}{R} \quad (1)$$

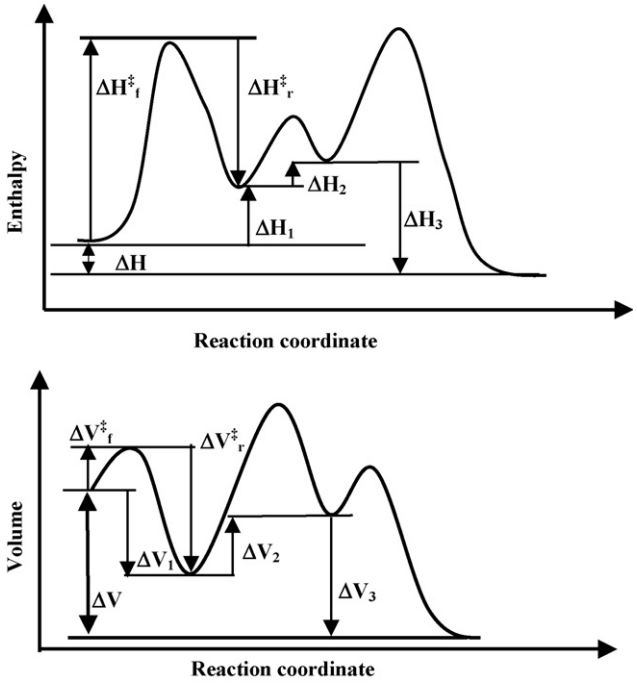


Fig. 6. Diagram showing volume and enthalpy profiles that can be obtained utilizing time-resolved photothermal methods.

where $k_b$ is Boltzman's constant, $h$ the Planck's constant, $k_{obs}$ is the observed rate constant, and $T$ is the absolute temperature) and:

$$-RT\left(\frac{\delta(\ln(k_{obs}))}{\delta P}\right)_T = \Delta V^{\ddagger} \quad (2)$$

where $R$ is the universal gas constant, $T$ the temperature and $P$ is the applied pressure [26,27]. The slope of the line in Eq. (1) gives the activation enthalpy while the intercept provides the entropy of activation. Likewise, the slope in Eq. (2) gives the activation volume. Determining the activation parameters for all of the pathways involved in a chemical reaction allows for the construction of a complete thermodynamic profile (see Fig. 6). The difficulty, however, arises from the fact that the activation parameters cannot always be determined in both the forward and reverse directions. Thus, to obtain the complete profile requires the knowledge of $\Delta H^{\ddagger}/\Delta V^{\ddagger}$ in one reaction direction as well as the overall $\Delta H/\Delta V$ for the given reaction step which requires determining $\Delta H/\Delta V$ for transient species along the reaction coordinate.

### 1.5. Steady-state thermodynamics

Equilibrium thermodynamic parameters can be easily obtained using the relationship between the Gibbs free energy and the equilibrium binding constant for various ligands (the van't Hoff equation) [28]:

$$\frac{\partial(\ln K)}{\partial(1/T)} = \frac{-\Delta H^{\circ}}{R} \quad (3)$$

where $K$ is the ligand association constant, $T$ the temperature, $R$ the gas constant, and $\Delta H^{\circ}$ is the reaction enthalpy. Similarly, the

change in molar volume for a given reaction can be determined from the pressure dependence of the equilibrium constant [26]:

$$\frac{\mathrm{d}(\ln K)}{\mathrm{d}P} = \frac{\Delta V^\circ}{RT} \tag{4}$$

where $P$ is the pressure. The equilibrium constant can be readily determined using the difference in the absorption spectrum between the ligand bound and unbound forms of the protein. For a simple ligand binding reaction:

$$P + L \leftrightarrow P : L \tag{5}$$

$$K_{\mathrm{eq}} = \frac{[P : L]}{[P][L]}. \tag{6}$$

Using $\Delta A_{\mathrm{abs}}$ at a wavelength giving a maximum difference between the bound and unbound forms of the protein the fraction of ligand bound protein can be expressed as:

$$Y = \frac{[P : L]}{[P] + [L]}. \tag{7}$$

Substituting the equilibrium constant gives:

$$Y = \frac{[L]}{(1/K_{\mathrm{eq}}) + [L]}. \tag{8}$$

Plotting $Y$ as a function of ligand concentration allows for the determination of $K_{\mathrm{eq}}$ [29]. The fractional concentration of ligand bound protein can also be monitored using Eq. (8) as a function of temperature/pressure to obtain the equilibrium thermodynamic parameters.

Using optical spectroscopy to probe thermodynamics of ligand binding in heme proteins have yielded a plethora of information regarding distal heme pocket modulation of ligand selectivity, binding affinity, catalytic activity, etc. Despite the success of these methods they are limited in probing only conformational changes/dynamics that effect the heme electronic state and cannot probe enthalpies/molar volume changes for very fast processes in which both forward and reverse rates cannot be measured (i.e., photolysis reactions, etc.). Photothermal methods including photoacoustic calorimetry, photothermal beam deflection, thermal lensing and transient grating spectroscopies have the advantage of being able to directly measure changes in heat as well as molar volume changes on fast timescales. Thus, these methods have the ability to probe conformational dynamics and other photochemical processes since they do not rely on changes in optical properties of any specific chromophore.

## 2. Theory behind photothermal methods

### 2.1. General background

Photothermal methods including photoacoustic calorimetry (PAC) and photothermal beam deflection (PBD) are proving to be powerful techniques for determining the magnitudes and time scales of molar volume and enthalpy changes associated with physiological events in proteins including folding/unfolding, electron transfer and ligand binding [30–37]. We have employed these methods to investigate nanosecond/millisecond thermodynamics associated with ligand photolysis from heme model systems, ligand binding to myoglobin and heme copper oxidases, and to the folding/unfolding of apo-myoglobin and several photochemically 'caged' peptides [38–52].

The physical principle behind both PAC and PBD is that a photo-excited molecule dissipates excess energy via vibrational relaxation to the ground state accompanied by thermal heating of the surrounding solvent [53,54]. Consider a region of solvent illuminated between $x = 0$ and $L$ that contains a population of molecular 'heat sources'. The response of the solvent to the heat impulse can be described mathematically by the classical heat equation:

$$\alpha\left(\frac{\partial^2 T}{\partial x^2}\right) + \left(\frac{\alpha}{k}\right) g(x,t) = \frac{\partial T}{\partial t}, \quad 0 < x < L,\ t > 0 \tag{9}$$

$$T(x, t=0) = F(x),\ T(x=0; t) = T_1,\ T(x=L, t) = T_2$$

where $\alpha$ is the thermal diffusivity, $k$ the thermal conductivity, $g(x,t)$ the heat deposited per unit volume and $F(x)$ is a function representing the initial solution temperature [54]. The solution to Eq. (9) is of the form:

$$\begin{aligned} T(x,t) = {} & \int F(x')G(x,t;x',\tau=0)\,\mathrm{d}x' \\ & + \left(\frac{\alpha}{k}\right)\int g(x';\tau)G(x,t|x',\tau)\,\mathrm{d}x'\,\mathrm{d}\tau \\ & + \alpha\int (T_1)\left.\frac{\partial G}{\partial x'}\right|_{x'=0}\mathrm{d}\tau - \alpha\int (T_2)\left.\frac{\partial G}{\partial x'}\right|_{x'=L}\mathrm{d}\tau \end{aligned} \tag{10}$$

where the integration limits over $x'$ are from $x' = 0$ to $L$ and over $\tau$ are from $\tau = 0$ to $t$, $G(x,t|x',\tau)$ represents the temperature response at point $x$ and time $t$ resulting from an instantaneous heat source released at point $x'$ and time $\tau$. Each integral is associated with a non-zero heating term including the initial condition, the energy generation, and terms for the boundry conditions. Considering the region being heated (and moving to cylindrical coordinates), the Green's function that solves the second integral in Eq. (10) is:

$$G(r', r, t) = (4\pi k t)^{-1} \exp\left[\frac{-(r^2 + r'^2)}{4Dt}\right] I_0\frac{r'r}{2Dt} I_0\frac{r'r}{2Dt} \tag{11}$$

where $D = k/C_p\rho$, $\rho$ the solution density and $C_p$ is the solution heat capacity. $I_0$ is a modified Bessel function of the first kind. The heat release function $g(r,t)$ is given as:

$$g(r,t) = \left(\frac{\alpha E_{\mathrm{a}}}{\hbar\omega}\right) I(r)\sum\nolimits_i \frac{\mathrm{d}Q_i(t)}{\mathrm{d}t} \tag{12}$$

where $\alpha$ is the absorption coefficient, $E_{\mathrm{a}}$ the total energy per pulse, $\hbar\omega$ the energy per photon, $I(r)$ the normalized pump pulse intensity distribution and $Q_i(t)$ is the total heat released by absorbing species $i$ at time $t$. For a laser pulse with a Gaussian

intensity distribution,

$$I(r) = \left(\frac{2}{\pi\omega_0^2}\right) \exp\left(\frac{-2r^2}{\omega_0^2}\right) \tag{13}$$

where $\omega_0$ is the full width at half maximum of the pump pulse. Evaluating Eq. (10) using Eqs. (11)–(13) gives the temperature change per excitation pulse as a function of the distance from the center of the Gaussian distribution as a function of time:

$$T(r,t) = \left(\frac{2\alpha E_a}{\pi\rho C_p \hbar\omega}\right)\left\{\frac{\exp[-2r^2/(8Dt+\omega_0^2)]}{8Dt+\omega_0^2}\right\}. \tag{14}$$

For solvents such as water, the heating described by Eq. (14) causes a rapid volume expansion within the illuminated volume resulting in both an acoustic wave and a change in solution index of refraction.

### 2.2. Photoacoustic calorimetry

In the case of photoacoustic calorimetry, the rapid change in solution temperature results in changes to the solution volume of the illuminated cylinder. The change in pressure at some point due to changes in solvent volume can be described by:

$$P = 2\pi f_a \nu_a \,\Delta x \rho \tag{15}$$

where $f_a$ is the frequency of the sound wave, $\nu_a$ the acoustic velocity, $\Delta x$ the volume displacement in one dimension, and $\rho$ is the solvent density [55,56]. The change in volume of a cylinder of radius $R$ and length $l$ due to an adiabatic, isobaric expansion can be written as:

$$\pi R^2 l - \pi(R+\Delta R)^2 l = \beta V\,\Delta T \tag{16}$$

where $\beta$ is the volumetric expansion coefficient. Using Eq. (14) and assuming a point source of heat (i.e., $r=0$ in Eq. (14)) then:

$$\pi R^2 l - \pi(R+\Delta R)^2 l = \beta V\left(\frac{2\alpha E_a}{\pi\rho C_p\hbar\omega}\right) \tag{17}$$

and for $\Delta R \ll R$:

$$\Delta R = \left(\frac{\beta}{C_p\rho}\right)\left(\frac{\alpha E_a R}{\pi\hbar\omega}\right). \tag{18}$$

The $\Delta R$ term in Eq. (18) is directly proportional to $\Delta x$ in Eq. (15) such that $\Delta x = B\,\Delta R$, where $B$ is a proportionality constant. Substituting Eq. (18) into Eq. (15) gives:

$$P = B2 f_a \nu_a \left(\frac{\beta}{C_p}\right)\left(\frac{\alpha E_a R}{\hbar\omega}\right) \tag{19}$$

For a fixed excitation system the $f_a$ and $R$ terms can be included in the proportionality constant $B$ giving:

$$P = B\left(\frac{\nu_a\beta}{C_p}\right)(\alpha E_0) \tag{20}$$

where $E_0$ is the total energy of the excitation pulse normalized to the photon energy.

The pressure change results in the generation of an acoustic wave in solution that is governed by the following wave equation:

$$\nabla^2\Psi(r,t) - \left(\frac{1}{\nu_s^2}\right)\frac{\partial^2\Psi(r,t)}{\partial t^2} = -4\pi h(r,t) \tag{21}$$

where $\nu_s$ is the speed of sound in the medium, $\Psi(r,t)$ the wave amplitude at the observation coordinates $r$ and $t$, and $h(r',t)$ is a heat source function [55]. The solution to this equation is of the form:

$$\Psi(r,t) = \left(\frac{1}{4\pi}\right)\int dt''\int dr'\, g(r,r',t,t')h(r,t') \tag{22}$$

where $g(r,r',t,t')$ is a Greens function that solves the wave equation for the given impulse heat function. At $r'=0$ (point source) the impulse function can be written in terms of a heat function as: $h(r',t') = \delta(r')f(t')$, where $\delta$ denotes the Dirac delta function and $f(t')$ describes the temporal behavior of the heat source. The solution to Eq. (22) gives the acoustic wave amplitude as:

$$\Psi(r_0,t) = \frac{f(t-(r_0/\nu_s))}{4\pi r_0}. \tag{23}$$

where the $r_0/\nu_s$ term is a propagation delay term and the $1/r_0$ is an energy conservation term associated with spherical emitters. For a single heat source transient with a lifetime $\tau$, $f(t')$ can be written as $(h_0\,e^{-t'/\tau}/\tau)\,\vartheta(t')$ where $\vartheta(t')$ is a Heaviside unit step function. The wave amplitude can now be written as:

$$\Psi(r_0,t) = \left(\frac{h_0}{4\pi r_0}\right)\left(\frac{e^{-t''/\tau}}{\tau}\right)\vartheta(t'). \tag{24}$$

The acoustic wave described by $\Psi(r_0,t)$ represents the wave amplitude observed at the transducer. The transducer response to the wave amplitude is that of an under-damped oscillator with an impulse response given by:

$$G(t,t'') = A\,\sin(\nu(t-t''))\,e^{-(t-t'')/\tau_0} \tag{25}$$

with an amplitude $A$, a characteristic oscillation frequency $\nu$ and a relaxation time $\tau_0$. The transducer response (piezoelectric crystal) is found by the convolution of the impulse response, $G(t,t'')$, with the acoustic amplitude, $\Psi(r_0,t'')$ giving:

$$V(t) = \int_{-\infty}^{t} G(t,t'')\Psi(r_0,t'')\,dt'' \tag{26}$$

Evaluation of Eq. (26) gives Eq. (27) for the transducer response:

$$V(t) = \left(\frac{h_0 A}{4\pi\rho_0}\right)\left(\frac{\nu\tau}{1+\nu^2\tau^2}\right) \times\left\{e^{-t/\tau} - e^{-t/\tau_0}\left[\cos(\nu t) - \left(\frac{1}{\nu t}\right)\sin(\nu t)\right]\right\} \tag{27}$$

where $\tau$ is the lifetime of the heat evolving process. Eq. (27) can be used to model the relationship between the lifetime of the heat evolving process and the amplitude at the transducer. The maximum transducer amplitude can be determined for cases in which $\tau \ll 1/\nu$ and for cases in which $\tau \gg 1/\nu$:

$$\left|V_{\max}\left(t \ll \frac{1}{\nu}\right)\right| \geq \left(\frac{h_0 A}{4\pi r_0}\right) e^{-t/\tau_0} \tag{28}$$

$$\left|V_{\max}\left(t \gg \frac{1}{\nu}\right)\right| \geq \left(\frac{h_0 A}{4\pi r_0}\right)\left(\frac{1}{\nu t}\right)(\mathrm{e}^{-t/\tau} + \mathrm{e}^{-t/\tau_0}). \quad (29)$$

In practice, the impulse heat sources are the molecules that we wish to probe. Photo-excitation of these molecules results in a transition from the ground electronic state to some higher excited state governed by Fermi's Golden Rule. Subsequent to excitation, the molecules may relax via emission of a photon (fluorescence), inter-system crossing to an excited triplet state or non-radiative decay back to the ground state. In addition, excited state molecules may undergo photochemical processes resulting in changes in molecular structure and/or bond cleavage/formation which can alter the molecular dimensions of the molecule(s) (i.e., changes in van der Waals volume) as well as alter the charge distribution of the molecule(s) in question (giving rise to electrostriction effects). The measured acoustic signal can be described as per Eq. (30), where $S$ is the acoustic signal (equivalent to the acoustic amplitude described in Eqs. (28) and (29)), $K$ an instrument response parameter, $E_a$ the number of Einsteins absorbed, $\Phi$ the quantum yield for the photochemical process, and $\Delta V_{th}$ and $\Delta V_{con}$ are the solution volume changes due to thermal expansion and solvation/molecular structural changes [54–56]. The solution volume changes due to heat returned to the solvent subsequent to excitation are described by the relationship in Eq. (31).

$$S = KE_a(\Delta V_{th} + \Delta V_{con}) \quad (30)$$

$$\Delta V_{th} = \left(\frac{\beta}{C_p \rho}\right) Q \quad (31)$$

The $\Delta V_{con}$ accounts for physical changes in van der Waals volume and/or solvation changes subsequent to photoexcitation. The contributions from $\Delta V_{th}$ and $\Delta V_{con}$ to the total signal, $S$, can be differentiated by examining the temperature dependence of the acoustic signal. Furthermore, use of a calibration compound in which $\Delta V_{con} = 0$ enables the instrument response parameter, $K$, to be eliminated by taking a ratio of the sample signal to the calibration signal. Letting $F(T) = (\beta/C_p\rho)$ ($\beta$ = coefficient of thermal expansion of the solvent ($K^{-1}$), $C_p$ = heat capacity (cal g$^{-1}$ K$^{-1}$), and $\rho$ = density (g mL$^{-1}$)) gives Eq. (32) for the (signal/reference) ratio, $\phi$, scaled to the energy of the absorbed photon. A plot of $\phi E_{h\nu}$ versus $1/F(T)$ gives a straight line with a slope equal to $\Delta V_{con}$ associated with a change in conformation and an intercept equal to the heat evolved ($Q$). Since $Q$ is the amount of heat released to the solvent associated with a reaction step, $(E_{h\nu} - Q)/\Phi = \Delta H$ for the reaction.

$$R = \Delta V_{\text{Reference}} = \left(\frac{\beta}{C_p \rho}\right) E_{h\nu} \quad (32)$$

$$\left(\frac{S}{R}\right) E_{h\nu} = \phi E_{h\nu} = \left(Q + \left(\frac{C_p \rho}{\beta}\right) \Delta V_{con}\right) \quad (33)$$

For reactions which involve multiple steps with time scales between ~50 ns and ~15 μs (for 2 MHz transducers), the individual contributions of $\Delta V_{con}$ and $Q$ for each kinetic step can be resolved (in this case, $\Delta H = -Q/\Phi$). For a two step reaction the observed time dependent acoustic signal results from a convolution of a time dependent volume source, $H(t)$, with an instrument response function, $T(t)$ as described in Eq. (34) and (35) with $k_i = 1/\tau_i$. Deconvolution of the signal involves estimating the parameters in $H(t)$ and convoluting the test $H(t)$ with $T(t)$ (acoustic signal of the reference compound). The parameters associated with $H(t)$ are varied until an appropriate chi-square value is obtained.

$$E(t)_{obs} = H(t) \times T(t) \quad (34)$$

$$H(t) = \phi_1 \exp\left(\frac{-t}{\tau_1}\right) + \left[\frac{\phi_2 k_2}{k_2 - k_1}\right] \times \left[\exp\left(\frac{-t}{\tau_1}\right) - \exp\left(\frac{-t}{\tau_2}\right)\right] \quad (35)$$

### 2.3. Photothermal beam deflection

Photothermal beam deflection detects changes in the refractive index subsequent to excitation by measuring the intensity of a probe laser beam that passes through the sample and is centered on a position sensing diode (the wavelength of the probe laser is outside the absorbance range of the sample). The pump laser (initiating the photochemistry) then passes nearly collinear with the probe laser. The magnitude of the resulting deflection of the probe laser on the position sensor is a measure of the refractive index change due to point source heating. The effect of temperature on the solution refractive index is given by:

$$n(r,t) = n_0 + \Delta n(r,t) = n_0 + \left.\frac{\partial n}{\partial T}\right|_{T\ \text{ambient}} T(r,t) \quad (36)$$

For a Gaussian light beam passing through the spatially varying refractive index (variation due to the point source heating) is given by:

$$\nabla_\perp n(r,t) = \frac{\mathrm{d}}{\mathrm{d}s}\left(\frac{n_0\, \mathrm{d}r_0}{\mathrm{d}s}\right) \quad (37)$$

where $\nabla_\perp n(r,t)$ is the gradient of the refractive index perpendicular to the direction of the beam propagation ($s$) and $r_0$ is a vector representing the path of the probe beam (i.e., displacement) perpendicular to the original propagation path. Since the displacement is small,

$$\frac{\mathrm{d}r_0}{\mathrm{d}s} \sim \phi = \left(\frac{1}{n_0}\right)\left(\frac{\partial n}{\partial T}\right)\int_{\text{path}} \nabla_\perp T(r,t)\, \mathrm{d}s \quad (38)$$

Using the expression for the temperature change induced by a point heat source (Eq. (14)) in Eq. (38) gives the angle of probe beam deflection from the direction of incidence:

$$\phi = \left(\frac{8\alpha E_a z}{\pi \rho C_p \hbar \omega}\right)\left(\frac{\partial n}{\partial T}\right)(r) \times \left[\frac{\exp[-2r^2/(8Dt + \omega_0^2)]}{(8Dt + \omega_0^2)^2}\right] \sum Q_i(t). \quad (39)$$

The change in refractive index can also be written in the form:

$$\Delta n = \Delta n_{th} + \Delta n_{pl} + \Delta n_{vol} \quad (40)$$

where the first term relates refractive index changes to changes in solvent density (due to heating), the second term relates to the 'population lens' which involves changes in refractive index due to the photo-production of new species in solution which affect the refractive index and the last term relates to changes in molar volume/solvation of the photoexcited species. The $\Delta n$ term in Eq. (40) relates directly to the angle of beam deflection given in Eq. (39). The first term can be evaluated by assuming that $(dn/dT)$ does not vary over the transient heating temperature change:

$$\Delta n_{\text{th}} = \int \left(\frac{dn}{dT}\right) dT$$
$$\Delta n_{\text{th}} \sim \left(\frac{dn}{dT}\right) \Delta T \tag{41}$$

Using Eq. (14) for the $\Delta T$ term and assuming: (1) a point heat source ($r=0$) and (2) no thermal diffusion on the observation time scale gives:

$$\Delta n_{\text{th}} \sim \left(\frac{dn}{dT}\right)\left(\frac{Q}{\rho C_p}\right) \tag{42}$$

where $Q$ is the thermal energy released to the solvent ($Q=\alpha E_a/h\nu$).

The $\Delta n_{\text{vol}}$ term can be expressed as:

$$\Delta n_{\text{vol}} = \int \left(\frac{dn}{dV}\right) dV = \int \left(\frac{dn}{d\varepsilon}\right)\left(\frac{d\varepsilon}{d\rho}\right)\left(\frac{d\rho}{dV}\right) dV. \tag{43}$$

The $(dn/d\varepsilon)$ term can be found using the fact that $n^2=\varepsilon$ giving $(dn/d\varepsilon)=(2n)^{-1}$. The corresponding $(d\rho/dV)$ term is evaluated using an ideal gas approximation in which $\rho=N/V$ giving $(d\rho/dV)=(d(N/V)/dV)=-N/V^2=-\rho/V$. The $(d\varepsilon/d\rho)$ term is derived from the Claussius–Messotti equation:

$$\left(\frac{d\varepsilon}{d\rho}\right) = \frac{(\varepsilon-1)(\varepsilon+2)}{3\rho} \tag{44}$$

where $\varepsilon$ is the solvent permittivity and $\rho$ is the density [57]. Substituting into Eq. (43) gives:

$$\left(\frac{dn}{d\varepsilon}\right)\left(\frac{d\varepsilon}{d\rho}\right)\left(\frac{d\rho}{dV}\right)$$
$$= -\left(\frac{1}{2n_0}\right)\left(\frac{-\rho}{V_{\text{solv}}}\right)\left(\frac{(\varepsilon-1)(\varepsilon+2)}{3\rho}\right)$$
$$= \left[\frac{(\varepsilon-1)(\varepsilon+2)}{6V_{\text{solv}}n_0}\right] \tag{45}$$

where $n_0$ is the refractive index of the unperturbed solvent. Integrating Eq. (45) gives (using $dV\sim\Delta V$ since the volume changes induced by excitation are small):

$$\int \left(\frac{dn}{d\varepsilon}\right)\left(\frac{d\varepsilon}{d\rho}\right)\left(\frac{d\rho}{dV}\right) dV$$
$$= \int \frac{(\varepsilon-1)(\varepsilon+2)}{6Vn}\, dV$$
$$= \frac{(\varepsilon-1)/(\varepsilon+2)}{6n}\int \frac{dV}{V} \sim \frac{(\varepsilon-1)(\varepsilon+2)}{6n_0(\Delta V/V)}. \tag{46}$$

Finally, the 'population lens' term, $\Delta n_{\text{pl}}$ is given as:

$$\Delta n_{\text{pl}} = \frac{(n_0^2+2)^2\alpha_i}{(18n_0\varepsilon_0)\,\Delta N} \tag{47}$$

where $\varepsilon_0$ is the vacuum permittivity, $N$ the number of excited molecules per unit volume, and $\alpha_i$ is the polarizability of the excited species. The population lens is related to changes in the absorption of the photoexcited molecules through the Kramers–Kronig transform. Thus, if the sample being probed using photothermal deflection exhibits an absorption change at the probe wavelength, then the corresponding refractive index will also change and contribute to $\Delta n$. In practice, the probe wavelengths are specifically chosen to be far from any anticipated absorption changes within the photoexicted molecules thus making the $\Delta n_{\text{pl}}$ term negligible. Substituting Eqs. (43) and (46) into Eq. (40) gives Eq. (48) for the overall change in deflection amplitude.

$$\text{Sample deflection} = AE_a\Phi\left\{\left(\frac{dn}{dT}\right)\left(\frac{1}{\rho C_p}\right)Q + \frac{(\varepsilon-1)(\varepsilon+2)}{6n_0(\Delta V/V)}\right\} \tag{48}$$

where $A$ is an instrument response parameter, $E_a$ the number of Einsteins absorbed, $\Phi$ the quantum yield for the photochemical process being investigated, $Q$ the amount of heat returned to the solvent subsequent to excitation and $\Delta V$ is the molar volume change associated with any photo-induced chemistry. It can be recognized that $[(\varepsilon-1)(\varepsilon-2)]/(6n_0)$ is actually $V(dn/dV)$ and thus Eq. (48) can be simplified to:

$$\text{Sample deflection} = AE_a\Phi\left\{\left(\frac{dn}{dT}\right)\left(\frac{1}{\rho C_p}\right)Q + \left[V\left(\frac{dn}{dV}\right)\right]\Delta V\right\} \tag{49}$$

As with PAC, the instrument response parameter $A$ can be eliminated by taking a ratio of the sample deflection to the deflection of a reference molecule in which $\Delta V=0$ and all of the absorbed photon energy is converted to heat within the laser pulse (i.e., $Q=E_{h\nu}$). In this case the reference deflection can be written as:

$$\text{Reference deflection} = AE_a\Phi\left[\left(\frac{dn}{dT}\right)\left(\frac{E_{h\nu}}{\rho C_p}\right)\right] \tag{50}$$

The ratio of sample deflection to reference deflection is then:

$$\left(\frac{S}{R}\right)E_{h\nu} = \Phi\left\{Q + \left(\frac{C_p\rho}{(dn/dT)}\right)\left(\frac{V\,dn}{dV}\right)\Delta V\right\} \tag{51}$$

Since the $(dn/dT)$ term is temperature dependent for water the values of $Q$ and $\Delta V$ can be found by measuring deflection amplitudes for both sample and reference as a function of $T$, scaling to the photon energy and plotting versus $[C_p\rho/(dn/dT)]$. The $V(dn/dV)$ term is relatively constant over the temperature ranges used in the PBD measurements. For example, at 10 °C $n_0=1.334$ giving a value for $\varepsilon$ of 1.78 and a $V(dn/dV)$ value of 0.37 and at 35 °C $n_0=1.332$ giving a value for $\varepsilon$ of 1.77 and a $V(dn/dV)$ value of 0.36. Thus, the molar volume change obtained from the $(S/R)E_{h\nu}$ versus $C_p\rho/(dn/dT)$ can be determined from slope/$[V(dn/dV)]\sim$ slope/0.365.

The parameters for individual reaction steps are analyzed by fitting the data to Eq. (52) where the $\alpha_i'$s are effectively equal to the ($S/R$) ratios given in Eq. (51) for each intermediate step:

$$F = \alpha_0 + \sum \alpha_i \left(1 - \exp\left[\frac{-t}{\tau_i}\right]\right) \quad (52)$$

where the $\tau_i$ are the lifetimes of the individual reaction steps and the $\alpha_i$ values are the corresponding normalized deflection amplitudes (see Fig. 8).

### 2.4. Instrumentation for PAC and PBD

#### 2.4.1. PAC

Photoacoustic calorimetry instruments vary in their design and what follows is a description of the instrument currently used in our laboratory (Fig. 7, top). In our laboratory, acoustic waves are generated from excitation of a sample by either 532 or 355 nm laser pulses (frequency doubled/tripled Continuum Minilite I, Q-switched Nd:YAG laser, 6 ns pulse, ~100 μJ pulse$^{-1}$). A 1 cm × 1 cm quartz cuvette containing 1 mL of a sample is placed on the center of an Panametrics V103 detector housed in a Quantum Northwest variable temperature cell holder. The optical density at the excitation wavelength is typically between 0.1 and 0.6. The temperature can be controlled to within 0.02 °C

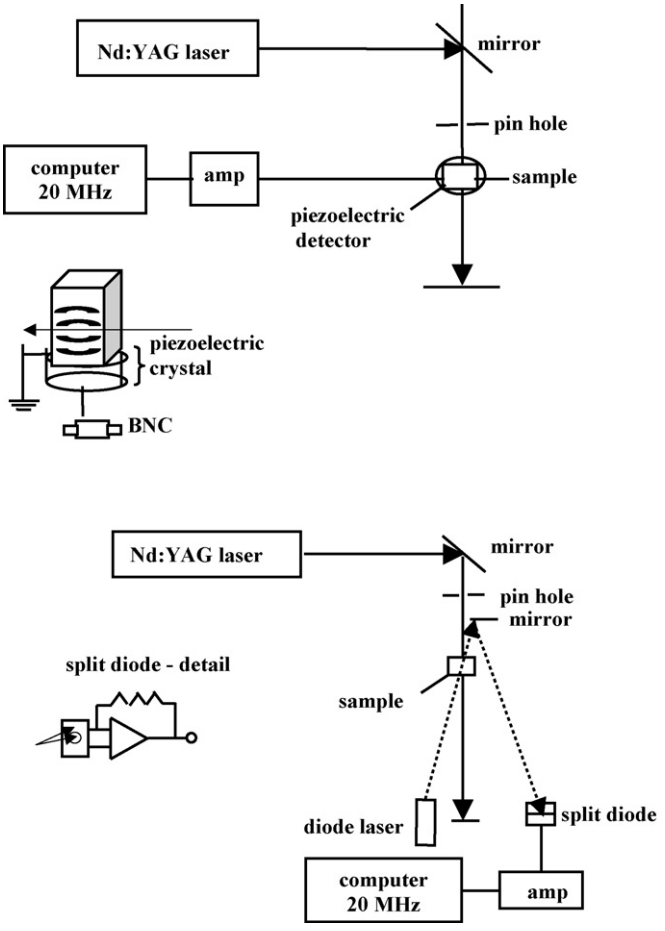


Fig. 7. Schematic diagram of both photoacoustic calorimtery and photothermal beam deflection instruments. Details are discussed in the text.

which is essential for minimizing the uncertainty in the $\phi E_{hv}$ versus ($C_p\rho/\beta$) plots. Contact between the cuvette and either detector is facilitated by a thin layer of vacuum grease. The acoustic waves created by photochemical reactions in the sample result in compression of the crystal and generation of a voltage that is amplified (ultrasonic preamplifier from Panametrics) and recorded by a NI 5102 15 MHz Oscilloscope controlled by Virtual Bench-Scope software (National Instruments). It is also important to note the photolysis power should be kept as low as possible to stay within a linear energy calibration range. It is assumed that the calorimetric reference absorbs only one photon during the duration of the laser pulse. Absorption of additional photons would result in a miss-calibration of the sample acoustic signal.

#### 2.4.2. PBD

The experimental setup of our PBD instrument is shown in Fig. 7, Bottom and is an adaptation of the PAC instrument described above. Nearly co-linear pump and probe beams are counter propagated through the center of the sample cuvette. The pump beam is the 532 nm/355 nm output of a Nd:YAG laser (Continuum Minilite I, 6 ns pulse, ~100 μJ). The probe beam is a continuous wave diode laser (Edmond Scientific, LDL 175, 820 nm, 3 mW) and its position is fixed with a pine hole (0.5 mm) placed before the sample cuvette. The mirror behind the sample is used to center the probe beam such that the intensity is distributed equally upon both sides of a split photodiode bicell detector (Centronic LD2-5T coupled with an Analog Devices AD844 amplifier operating in a difference mode) which is fed into a 200 MHz amplifier of our own design. The generated deflection signal is then digitized by a National Instruments NI 5102 15 MHz Oscilloscope controlled by Virtual Bench-Scope software (National instrument).

## 3. Photothermal studies of CO binding to heme model systems

Thermodynamic studies of interactions of synthetic heme model complexes with small gaseous ligands such as $O_2$, CO, and NO have significantly advanced our understanding of ligand recognition and structure-function relationship in heme proteins. To mimic the active site of dioxygen-carrying hemoprotein, numerous approaches have been taken to synthesize high-spin five-coordinate $Fe^{II}$ porphyrins with a nitrogen-based aromatic ligand [58–60]. These approaches include: (i) "chelated hemes" with covalently attached axial imidazole to the heme periphery [60]; (ii) "picket fence hemes" having steric shielding on one face of the porphyrin ring [59]; (iii) "heme base mixtures" with base to be a sterically hindered ligand, such as 2-methylimidazole [58]. Binding of diatomic ligands to such complexes has been extensively studied by laser flash photolysis on a femto- to millisecond timescale and those studies provided a description of events localized near the heme group [59]. Subsequent to photolysis of iron-ligand bond, iron atom quickly moves ($\tau < 1$ ps) out of the porphyrin plane, which is followed by a porphyrin ring doming. On the picosecond to nanosecond timescale, the free ligand may either rebind to the heme iron in

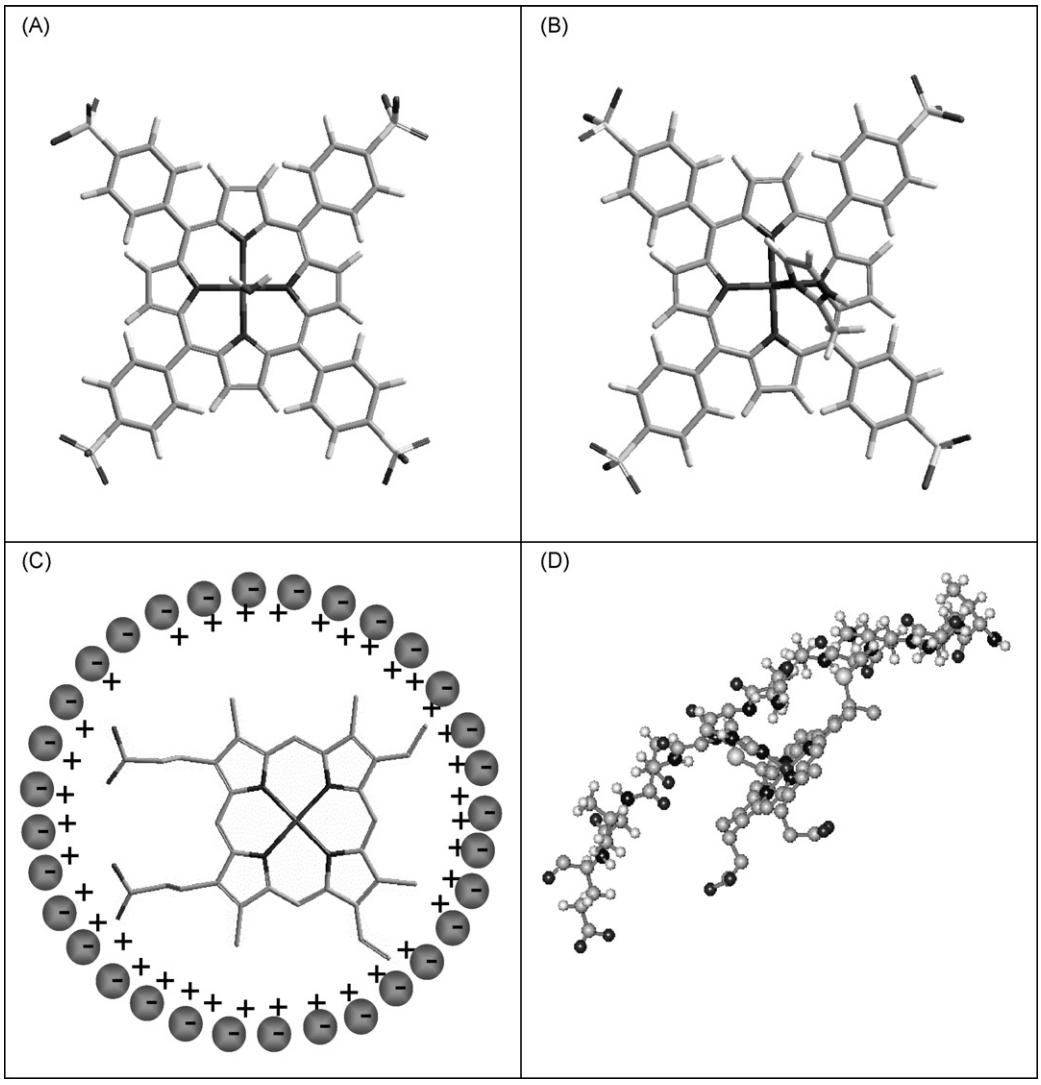


Fig. 8. Schematic presentation of heme model complexes: $(H_2O)Fe^{II}4SP$ is shown in (Panel A); (2-MeIm)$Fe^{II}4SP$ in (Panel B); $Fe^{II}PPIX$ in a micelle is depicted in (Panel C); MP-11 is shown (Panel D).

a geminate recombination process or move out from the solvent cage. In the later case, the subsequent rebinding from the bulk solvent occurs on the microsecond to millisecond timescale.

To obtain insight into the thermodynamics of ligand rebinding we have applied PAC, PBD and transient absorption spectroscopy to construct complete thermodynamic profiles for CO association to several heme model complexes (Fig. 8). First we have studied Fe(II) protoporphyrine IX ($Fe^{II}PPIX$) in cetylmethylammonium bromide (CTAB) micelles [39]. Since the dimension of the CTAB micelle is similar to that of myoglobin, and each micelle contains a single $Fe^{II}PPIX$ molecule [61,62], the $Fe^{II}PPIX$ in CTAB micelle system represents a very simple model to mimic myoglobin. Subsequently, we have investigated CO binding properties to a water soluble $Fe^{II}$ *meso*-tetrakis(4-sulfonatophenyl)-porphyrine ($Fe^{II}4SP$) having a water molecule ($(H_2O)Fe^{II}4SP$) or 2-methylimidazole ((2-MeIm)$Fe^{II}4SP$) in the position of axial ligand [48]. We have also determined thermodynamic parameters for CO association to a natural chelated heme, microperoxidase -11 ($Fe^{II}$MP-11). MP-11 is an 11 residue heme-binding peptide with the heme covalently bound to the peptide via a thioether linkage and coordination through a histidine residue [63]. Photolysis of CO heme complexes show no evidence for geminate recombination and displays a quantum yield of unity [60].

Steady state UV–vis absorption spectra, specifically Soret band and visible Q bands, are characteristic of the spin and coordination state of heme. $Fe^{II}PPIX$ in CTAB micells is found to be four-coordinate as judged from the Soret band with three maxima at 409, 420, and 440 nm. Upon CO binding, $Fe^{II}PPIX$ undergoes a transition to low-spin six-coordinate with a water molecule to be the sixth ligand. Its absorption spectrum has the maximum of the Soret band located at 403 nm and two visible bands at 530 and 563 nm. On the other hand, $Fe^{II}4SP$ in water or in the presence of 50 mM 2-MeIm has an absorption spectrum characteristic of the high-spin five-coordinate heme with a broad visible band centered around 560 nm and the Soret band situated at 426 and 433 nm for $(H_2O)Fe^{II}4SP$ and for (2-MeIm)$Fe^{II}4SP$ complex, respectively. Saturation with CO

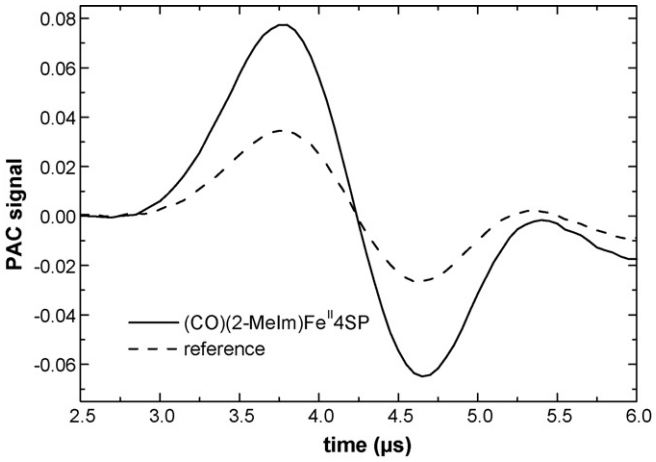


Fig. 9. Typical photoacoustic trace for CO photodissociation from (CO)(2-MeIm)Fe$^{II}$4SP and reference (Fe$^{III}$4SP in 50 mM Tris buffer pH 7) at 22 °C. The sample is shown as a solid line and the reference as dashed line. The absorbance of sample and the reference was 0.35 ± 0.02 at 532 nm.

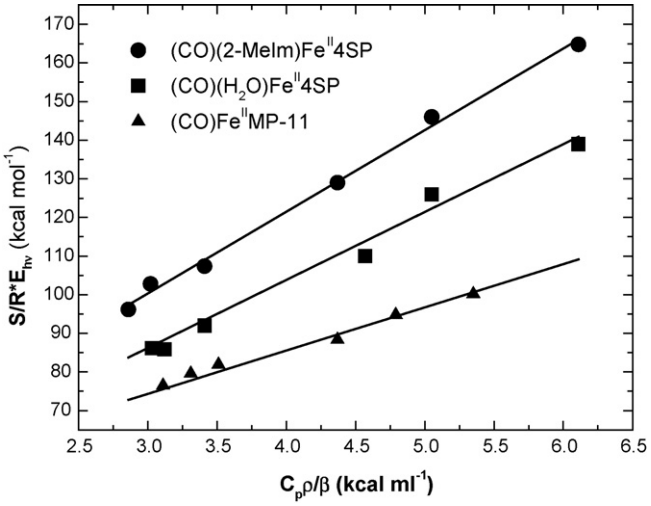


Fig. 10. Plot of $S/R\,E_{hv}$ vs. $(C_p\rho\beta)$ for CO photodissociation from (CO)Fe$^{II}$4SP, (CO)(H$_2$O)Fe$^{II}$4SP and (CO)Fe$^{II}$MP-11 complexes.

results in the blue shift of the Soret band to 415 nm and 417 nm for the (CO)(H$_2$O)Fe$^{II}$4SP, and (CO)(2-MeIm)Fe$^{II}$4SP complex, respectively, in agreement with the formation of the low-spin six-coordinate heme. The absorption spectrum of Fe$^{II}$MP-11 exhibits a Soret band at 416 nm and two visible peaks at 520 and 550 nm indicating that the heme in Fe$^{II}$MP-11 is low-spin six-coordinate with the proximal ligand to be His18 and the distal ligand likely to be the terminal amino group of the same molecule and/or aggregation of different Fe$^{II}$MP-11 molecules [63]. The absorption spectrum of CO bound Fe$^{II}$MP-11 exhibits a Soret band at 412 nm and two visible bands at 529 and 613 nm in agreement with the presence of the six-coordinate low spin heme with CO being the distal ligand.

Reaction volume and enthalpy changes associated with CO dissociation from the heme complexes were determined by PAC. Fig. 9 shows the overlay of acoustic traces for CO photo-release from (CO)(2MeIm)Fe$^{II}$4SP and for the reference compound at 22 °C. The sample acoustic trace exhibits a larger amplitude (difference between the first maximum and minimum in the signal) compared to the reference trace that indicates the presence of volume and enthalpy changes associated with ligand release. The absence of a phase shift in the sample acoustic wave relative to the reference wave points out that the observed volume and enthalpy changes occurs within 50 ns. From the temperature dependence of the amplitude of the sample trace scaled to the amplitude of the reference trace, integrated values for the volume and enthalpy change were determined using Eq. (33). The plot of $\phi E_{hv}$ versus $(C_p\rho/\beta)$ is shown in Fig. 10 for (CO)(H$_2$O)Fe$^{II}$4SP, (CO)(2MeIm)Fe$^{II}$4SP, and (CO)Fe$^{II}$MP-11. The slope of the plot corresponds to the volume change and the intercept represents the amount of heat released to the solvent. The reaction enthalpy change was then calculated using $E_{hv} - Q = \Delta H/\Phi$. Extrapolated reaction volume and enthalpy changes for all four complexes are listed in Table 1.

Volume and enthalpy changes on the microsecond to millisecond timescale were determined using PBD. Fig. 11 shows a typical PBD trace for CO photodissociation from the

Table 1
Volume and enthalpy changes for CO dissociation from heme model complexes determined by PAC

| | $\Delta V$ (mL mol$^{-1}$) | $\Delta H$ (kcal mol$^{-1}$) |
|---|---|---|
| Fe$^{II}$PPIX | 3.1 ± 0.3 | −10 ± 1 |
| (CO)(H$_2$O)Fe$^{II}$4SP | 18.0 ± 1.0 | 20 ± 4 |
| (CO)(2MeIm)Fe$^{II}$4SP | 21.1 ± 0.7 | 17 ± 3 |
| (CO)Fe$^{II}$MP-11 | 11.2 ± 0.9 | 13 ± 3 |

(CO)(2MeIm)Fe$^{II}$4SP complex together with the trace for reference compound (Fe$^{III}$4SP in 50 mM Tris, pH 7). The fast increase in the reference PBD signal ($\tau < 10$ μs) corresponds to the prompt heat release due to the thermal relaxation subsequent to laser excitation. The PBD signal remains constant for more than 100 ms and then the signal decays back to the base line due to heat diffusion from the illuminated region. On the other hand, the sample trace shows two distinct phases. Initially, there

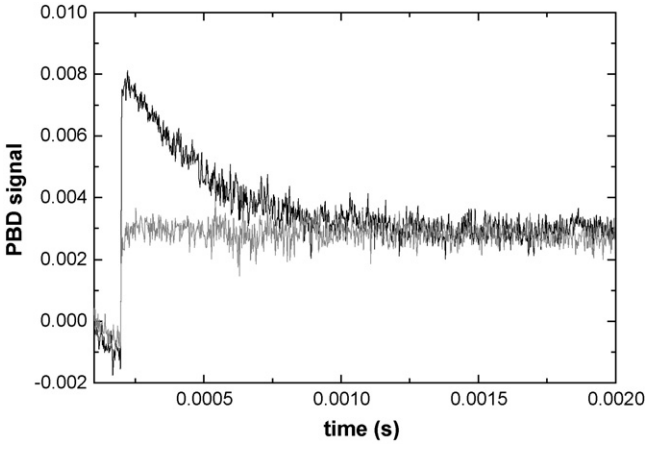


Fig. 11. PBD trace for CO photodissociation from (CO)(2-MeIm)Fe$^{II}$4SP and the reference compound (Fe$^{III}$4SP). The sample trace is shown in black and the reference trace in gray.

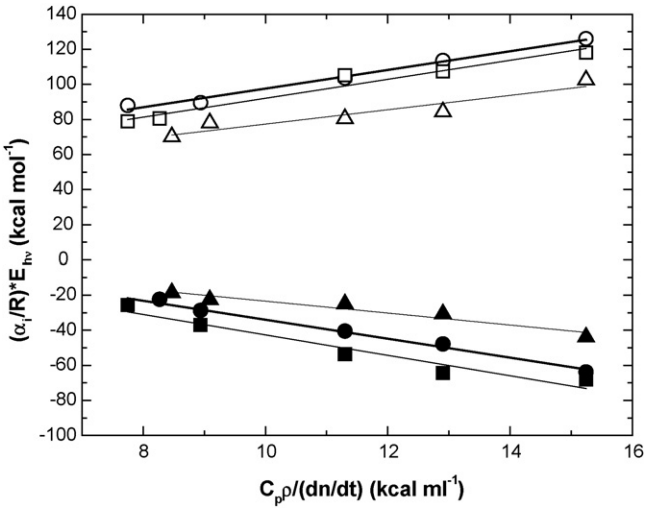


Fig. 12. The plot of $\alpha_i/RE_{h\nu}$ vs. $C_p\rho/(dn/dt)$ for CO photodissociation from and rebinding to $(H_2O)Fe^{II}4SP$ (circles), (2-MeIm)$Fe^{II}4SP$ (squares), and $Fe^{II}MP$-11 (triangles). $\alpha_i$ for the fast phase is shown as open symbols and $\alpha_i$ for the slow phase is shown as solid symbols.

is a fast increase in the amplitude ($\tau < 10\,\mu s$) which is followed by a single exponential decay on the microsecond timescale. On a longer timescale the sample trace matches the reference trace, in agreement with the reversibility of the process. PBD traces recorded for $(H_2O)Fe^{II}4SP$ and $Fe^{II}MP$-11 display similar pattern to those measured for (2-MeIm)$Fe^{II}4SP$. Plots of $\alpha_i E_{h\nu}$ versus $C_p\rho/(dn/dt)$ are shown in Fig. 12 and the extrapolated volume and enthalpy changes are listed in Table 2. The fast phase of sample signal corresponds to the CO photodissociation from the model complex and the volume and enthalpy changes determined from the amplitude of the fast phase match those observed by PAC. The slow phase represents CO rebinding to the heme complexes. In agreement with the reversible reaction, the volume and enthalpy changes determined for the CO rebinding have same absolute value but the opposite sign with respect to those measured for CO photodissociation. From the fit of the slow phase to Eq. (52), the rate constants for CO rebinding to heme model complexes were determined and correspond to those measured for CO rebinding using transient absorption spectroscopy [64,65]. The activation enthalpy and entropy parameters for CO rebinding to the model complexes were determined using Eyring plots and are listed in Table 2.

Previous studies have suggested that CO association to heme model complexes proceeds through a direct association pathway with the ligand rebinding directly to the high-spin six-coordinate heme or base elimination mechanism [60]. In the later case, CO

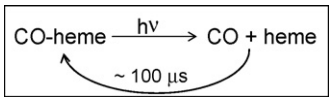


Scheme 1.

dissociation is accompanied by the loss of proximal base due to its lower affinity of unliganded heme compared to the heme–CO complex. Subsequently CO rebinds to the four-coordinate heme and is followed by base association on the millisecond timescale [26]. Our data show that no volume or enthalpy changes were detected on ~50 ns to ~10 μs timescale in PAC measurements and only single kinetic phase was observed in PBD measurements on the microsecond timescale. The rate constants and the activation parameters determined from this microsecond decay match those determined for CO rebinding in TA measurements suggesting that CO association to $(H_2O)Fe^{II}4SP$, (2-MeIm)$Fe^{II}4SP$, and $Fe^{II}MP$-11 complexes proceed through a direct association mechanism as shown in Scheme 1. This is further confirmed by the thermodynamic data. The observed reaction enthalpy change for those complexes is comparable to enthalpy change determined previously for CO binding to chelated hemes ($\Delta H = 17\,kcal\,mol^{-1}$) [60] and is consistent with the model in which only CO dissociates and subsequently rebinds to the heme.

Interpretation of the observed reaction volume changes is more complex. In general, reaction volume changes can be described as a sum of three contributions: (i) changes in van der Waals volume ($\Delta V_{vdW}$) due to the changes in bond lengths and angles; (ii) volume changes due to electrostriction ($\Delta V_{el}$); and solvation volume changes ($\Delta V_{sol}$) which results from differences of solvent packing around the reactants and products [50]. In the case of CO dissociation from heme complexes, $\Delta V_{el} = 0$ and therefore only $\Delta V_{vdW}$ and $\Delta V_{sol}$ contribute to the observed reaction volume change. The observed expansion ($\Delta V = \sim 17\,mL\,mol^{-1}$ for $Fe^{II}4SP$ complexes and $\Delta V = \sim 11\,mL\,mol^{-1}$ for $Fe^{II}MP$-11) originates in volume changes due to the Fe–CO bond cleavage and low-spin to high-spin heme transition. Previous studies on small complexes have estimated the reaction volume change for covalent bond cleavage to be 5–10 mL mol$^{-1}$ [66,67]. In such cases, the transition from the low-spin to high-spin heme accounts for roughly ~8 mL mol$^{-1}$. Comparable values ($\Delta V = 5$–$15\,mL\,mol^{-1}$) have been reported for low-spin to high-spin interconversion of $Fe^{II}$tris(2-(2-pyridyl)imidazole) and $Fe^{II}$tris(2-(2-pyridyl)-benzimidazole) in various solvents [67]. Structural changes which are associated with the spin transition involve displacement of the iron atom from the porphyrin

Table 2
Reaction and activation volume and enthalpy changes for CO photodissociation ($\Delta V_{fast}$ and $\Delta H_{fast}$) and rebinding ($\Delta V_{fast}$, $\Delta H_{fast}$ and $\Delta V^{\ddagger}$) to heme model complexes

| | $\Delta V_{fast}$ (mL mol$^{-1}$) | $\Delta H_{fast}$ (kcal mol$^{-1}$) | $\Delta V_{slow}$ (mL mol$^{-1}$) | $\Delta H_{slow}$ (kcal mol$^{-1}$) |
|---|---|---|---|---|
| $(CO)(H_2O)Fe^{II}4SP$ | 16 ± 1 | 9 ± 4 | −17 ± 2 | −20 ± 3 |
| (CO)(2MeIm)$Fe^{II}4SP$ | 17 ± 2 | 10 ± 7 | −18 ± 3 | −16 ± 9 |
| (CO)$Fe^{II}MP$-11 | 12 ± 3 | 17 ± 6 | −11 ± 2 | −11 ± 6 |

Reaction parameters were determined using PBD whereas activation volume changes were determined from pressure dependence of rate constant for CO rebinding.

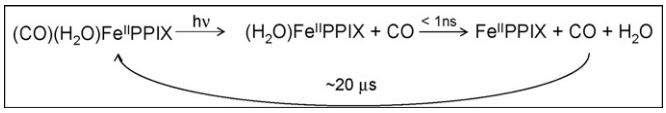


Scheme 2.

plane and contraction of the porphyrin ring. The volume change associated with these structural changes has been estimated to be 0.2–0.3 mL mol$^{-1}$ [67] and therefore cannot explain the volume change of 7–12 mL mol$^{-1}$ associated with the spin transition. On the other hand, perturbation of the solvent molecules structure as a result of the spin transition is likely to contribute to the positive volume change. In the case of MP-11, the presence of a polypeptide fragment may partially reduce the solvent perturbation as evident from the smaller volume change determine from the CO dissociation reaction. Solvation of CO molecules is not expected to contribute significantly to the observed volume changes since CO is partially solvated in the heme complexes.

The ligand dissociation from Fe$^{II}$PPIX in CTAB micelles is associated with significantly smaller volume and enthalpy changes ($\Delta V = 3.1$ mL mol$^{-1}$ and $\Delta H = -10.4$ kcal mol$^{-1}$) compared to Fe$^{II}$4SP and MP-11 systems [39]. In the micelle, the ligand dissociation was suggested to proceed through a base elimination mechanism as shown in Scheme 2. Transient absorption data have shown that CO photorelease is followed by dissociation of a water molecule occurring within 100 ns. Only a single process on longer timescales and it was proposed that CO and a water molecule rebind simultaneously to the four-coordinate Fe$^{II}$PPIX [48]. The observed enthalpy change can be expressed as: $\Delta H = \Delta H_{CO} + \Delta H_{H_2O}$, where $\Delta H_{CO}$ and $\Delta H_{H_2O}$ represent enthalpy change associated with CO dissociation from (CO)(H$_2$O)Fe$^{II}$PPIX and enthalpy change for H$_2$O dissociation from the high-spin five-coordinate (H$_2$O)Fe$^{II}$PPIX complex, respectively. Using $\Delta H_{CO}$ determined for CO dissociation from (CO)(H$_2$O)Fe$^{II}$4SP complex, $\Delta H_{CO} = \sim 16$ kcal mol$^{-1}$, and the observed enthalpy change, $\Delta H = -10$ kcal mol$^{-1}$, the enthalpy change for H$_2$O dissociation is estimated to be approximately $-26$ kcal mol$^{-1}$ suggesting that water molecule dissociation from five-coordinate high-spin heme is enthalpy driven. In a similar way the observed volume change can be expressed as a sum of two contributions, $\Delta V = \Delta V_{CO} + \Delta V_{H_2O}$, where $\Delta V_{CO}$ is the volume change associated with CO dissociation from the low-spin six-coordinate complex and $\Delta V_{H_2O}$ represents the volume change for H$_2$O dissociation from the high-spin five-coordinate (H$_2$O)Fe$^{II}$PPIX. Using $\Delta V = 3.1$ mL mol$^{-1}$ and $\Delta V_{CO} = 17$ mL mol$^{-1}$, which was measured for CO dissociation from (CO)(H$_2$O)Fe$^{II}$4SP complex, $\Delta V_{H_2O}$ is estimated to be approximately $-14$ mL mol$^{-1}$. It is unlikely, that breaking the Fe–OH$_2$ bond and concomitant transition from five-coordinate to four-coordinate heme iron would be result in such negative volume change since the fragmentation reactions are expected to be associated with the positive volume change [67]. On the other hand, since the dissociation takes place within CTAB micelles it is likely that the micellar environment restricts the extent of the volume changes which are associated with the cleavage of Fe–CO and Fe–OH$_2$ bonds and well as of volume changes due to the reorganization of solvent molecules which leads to the small volume change measured for CO and H$_2$O dissociation from the (CO)(H$_2$O)Fe$^{II}$PPIX complex in CTAB micelle.

## 4. Myoglobin

Ligand binding to myoglobin has been extensively investigated in order to understand the mechanism of small molecule binding in heme proteins [68]. Myoglobin, a small oxygen storage protein localized primarily in muscle cells of mammals, contains an iron protoporphyrin IX prosthetic group coordinated to the protein via a proximal histidine residue. The sixth iron coordination site is vacant in the physiologically relevant ferrous form and can be occupied by small diatomic molecules, such as oxygen, carbon monoxide, and nitric oxide. The mechanism of ligand binding to the heme iron has been investigated by time-resolved spectroscopy [69–73], X-ray crystallography [74] as well as with site directed mutagenesis [75–78]. Although O$_2$ is the physiological ligand, studies involving CO is often preferred since the stretching modes of CO absorb strongly in the mid-infrared region and the Fe–CO bond can be photolyzed with a quantum yield of unity allowing synchronous investigation of the rebinding reaction. It has been proposed that CO dissociation involves at least two intermediates and can be described according to the Scheme 3 where [Mb:CO] represents a geminate pair with the Fe–CO bond cleaved and CO located in the "primary docking site", and [Mb::CO] describes an intermediate with the ligand trapped in a more distant location from the active site which is referred to as the "secondary docking site" [78]. Since the crystallographic data show that the protein matrix is tightly packed in Mb without a direct pathway connecting the heme binding site to the surrounding solvent, protein motions or fluctuations are essential for the ligand to diffuse to and from the active site [79]. Structural fluctuations could create transient channels that allow for specific ligand trajectories was proposed on the basis of molecular dynamic simulations and such fluctuations necessarily results in change in protein volume [80].

Peters and collaborators have used PAC to investigate volume changes associated with ligand dissociation from Mb more than 15 years ago [81–83]. These Authors reported that CO dissociation from horse heart myoglobin (hhMb) is associated with an initial volume decrease of $-1.2$ mL mol$^{-1}$ and an enthalpy change of 7.4 kcal mol$^{-1}$. This initial contraction is followed by an endothermic expansion ($\Delta H = 7$ kcal mol$^{-1}$ and $\Delta V = 14$ mL mol$^{-1}$) with a lifetime of 700 ns [81]. The 700 ns phase which had not been observed by flash photolysis techniques, was also observed in the case of CO photodissociation from sperm whale myoglobin (swMb) although smaller volume changes were observed for the two phases [82]. The Authors proposed that the disruption of a salt bridge between Lys45 (Arg45 in sperm whale Mb) and the heme propionate side chain takes

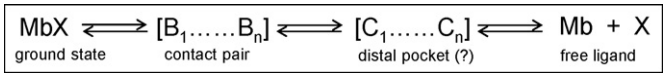


Scheme 3.

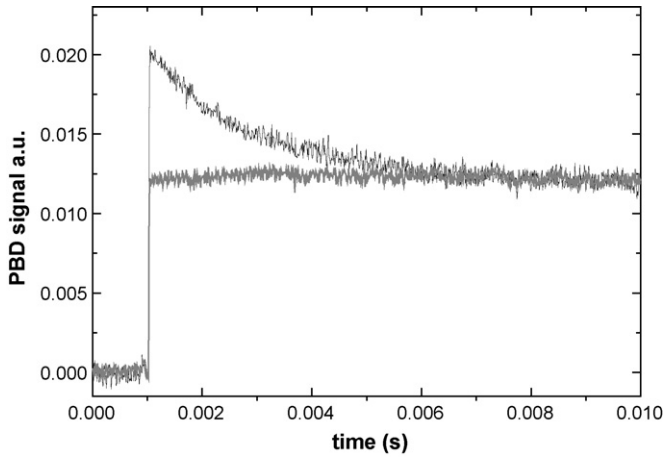


Fig. 13. The overlay of PBD trace for CO rebinding to deoxyMb (dark line) and for the reference compound (gray trace) measured at 18 °C.

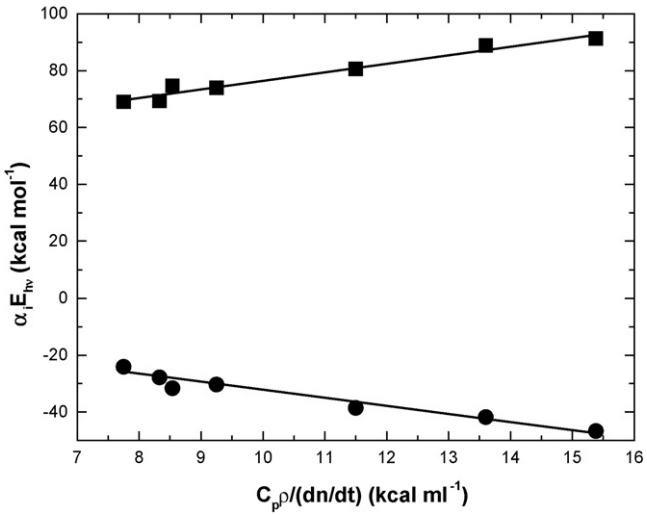


Fig. 14. The plot of $\alpha_i E_{hv}$ vs. $(C_p\rho)/(\mathrm{d}n/\mathrm{d}t)$ for the fast and slow phase (squares and circles, respectively).

place upon Fe–CO bound dissociation accounts for the initial volume and enthalpy changes. The subsequent 700 ns process was attributed to CO diffusion out of the protein matrix and the observed volume and enthalpy changes were associated with changes in protein conformation [83].

Recently, Angeloni and Feis have published a detailed photoacoustic study of CO photodissociation from myoglobin at neutral and acidic pH [84]. At pH 8, ligand dissociation from hhMb was described as a three-step process. The first step, which occurs faster than 20 ns and exhibits enthalpy change of 14 kcal mol$^{-1}$, was associated with Fe–CO bound cleavage. No significant volume changes were reported for this process. On the nanosecond timescale, two additional steps were identified. An exothermic process ($\Delta H = -3$ kcal mol$^{-1}$ and $\Delta V = -3$ mL mol$^{-1}$) with a lifetime of ~80 ns was attributed to ligand migration to a docking site on the heme proximal side. This process is followed by a volume expansion of 19 mL mol$^{-1}$ and an enthalpy change of 6 kcal mol$^{-1}$ with a lifetime of 800 ns. This event was attributed to CO migration into the bulk solvent. On the other hand, CO photodissociation at pH 3.5 was reported to be a two-step process with the slower phase occurring with a lifetime of 230 ns. The acceleration of CO release to the solvent was attributed to the fact that at low pH a significant fraction of myoglobin is in an "open conformation" with the distal histidine residue (His64) being protonated and swung out of the pocket toward the bulk solvent.

The studies described above have focused on CO photorelease from myoglobin but significantly less is known about the kinetics and energetics of structural changes which are associated with the ligand rebinding. Fig. 13 shows PBD traces for both CO rebinding to deoxyMb and the $Fe^{II}$4SP reference at 18 °C. The sample trace exhibits a fast increase in amplitude that occurs faster than ~10 μs and this phase is followed by a slow phase occurring on the ms timescale. The volume and enthalpy changes occurring faster than 10 μs were determined from the temperature dependence of the fast phase amplitude and the volume and enthalpy changes corresponding to the slow phase were obtained from the amplitude of the slow phase and a plot of $\alpha_i E_{hv}$ versus $C_p\rho/(\mathrm{d}n/\mathrm{d}t)$ as shown in Fig. 14. The corresponding thermodynamic parameters are listed in Table 3 [42]. The volume and enthalpy changes observed for the fast phase correspond to the sum of the volume and enthalpy changes determined previously by PAC confirming that the fast phase describes CO photodissociation and release into the bulk solvent. The slow phase exhibits a single exponential decay with the rate constant identical to that determined for CO rebinding by transient absorption spectroscopy ($k_{obs} = 5 \times 10^2$ s$^{-1}$ at 1 mM CO and 20 °C) [72].

The measured enthalpy change for CO rebinding to deoxyMb is approximately 10 kcal mol$^{-1}$ smaller than that determined for photodissociation of Fe–CO bond in heme model complexes ($\Delta H = -17$ kcal mol$^{-1}$) indicating that conformational changes that are associated with the ligand rebinding are endothermic with $\Delta H \sim 10$ kcal mol$^{-1}$. The extent of the conformational change can be estimated from the observed reaction volume change described by:

$$\Delta V = V_{\mathrm{Mb–CO}} - (V_{\mathrm{Mb}} + V_{\mathrm{CO}}) \quad (53)$$

where $\Delta V$ represents the reaction volume change, $V_{\mathrm{Mb–CO}}$ the partial molar volume of CO bound Mb, $V_{\mathrm{Mb}}$ the partial molar volume of Mb and $V_{\mathrm{CO}}$ the molar volume of CO. From the value of partial molar volume of CO in water, $V_{\mathrm{CO}} = 35$ mL mol$^{-1}$ [85]

Table 3
Thermodynamic parameters for CO photodissociation and rebinding to hhMb determined by PBD

| | $\Delta V$ (mL mol$^{-1}$) | $\Delta H$ (kcal mol$^{-1}$) | $\Delta H^{\ddagger}$ (kcal mol$^{-1}$) | $\Delta S^{\ddagger}$ (cal mol$^{-1}$ K$^{-1}$) |
|---|---|---|---|---|
| Fast phase ($\tau < 10$ (s) | 9.3 ± 0.8 | 7.4 ± 2.8 | n.d. | n.d. |
| Slow phase ($\tau \sim$ ms) | −8.6 ± 0.9 | −5.8 ± 2.9 | 7.1 ± 0.8 | −22.4 ± 2.8 |

and the observed reaction volume change ($\Delta V \sim -9\,\mathrm{mL\,mol^{-1}}$), the volume change coupled to change in myoglobin volume ($V_{protein} = V_{Mb–CO} - V_{Mb}$) is estimated to be $\sim 25\,\mathrm{mL\,mol^{-1}}$. Changes in protein volume during ligand association may reflect changes in hydration, packing and dynamics of the protein matrix [86]. Alignment of the crystal structure of the deoxy and CO bound Mb provides insight into the origin of the observed increase of Mb volume upon CO binding. Kachalova et al. [87] have reported that the most significant conformational difference between the structures of ligand-free and CO-bound Mb lay in the orientation of the heme with respect to E and F α-helices. Such scissor-like motion of the α-helices together with rearrangement of the heme binding pocket which includes the swinging of the distal histidine residue and passage of a water molecule into the solvent, may account for the observed positive volume change.

## 5. Thermodynamics of signaling in FixL

Bacteria employ two component signaling pathways to regulate diverse cellular processes in response to changes in external environment. In rhizobial species, an oxygen-responsive sensory/signaling system composed of two components, FixL–FixJ, controls expression of the genes required for nitrogen fixation, microaerobic respiration, anaerobic nitrate/nitrite respiration and hydrogen metabolism [88,89]. FixL proteins from two bacterial strains *Bradorhizobium japonicum* (*Bj*FixL) and *Sinorhizobium meliloti* (*Sm*FixL) have been intensively studied using biochemical and biophysical techniques [90–92]. *Sm*FixL and *Bj*FixL both contain an N-terminal sensory domain and a histidine kinase domain at the C-terminal end. The sensory domain binds a single molecule of heme (protoporphyrine IX). In the presence of molecular oxygen, the ferrous oxyheme complex inhibits enzymatic activity of the kinase domain whereas under anaerobic or semi-anaerobic conditions, oxygen dissociates from heme leading to the activation of the kinase domain, transphosphorylation of FixJ regulator and transcription of corresponding genes.

To date, a crystal structure of the full length protein has not been obtained although structures of the isolated heme domain in the presence of various distal ligands have been resolved and provided valuable insight into the mechanism of signal recognition [93–98]. The heme domain of FixL belongs to the Per–Arnt–Sim (PAS) domain structural super-family with a characteristic α/β-fold. The heme resides between a 16-residue long F α-helix and two β-strands and is linked to the protein through a proximal histidine residue (His200 in *Bj*FixL) (Fig. 15). The most recent model describing signal triggering is based primarily on the crystal structure of deoxy and $O_2$-bound FixL [95]. Superposition of these structures reveals that upon ligand binding the loop linking the proximal F (-helix and the G β-strand (FG loop) undergoes a shift of ∼1.6 Å. According to the model, oxygen binding to the heme iron leads to a high-spin five-coordinate to low-spin six-coordinate heme transition which is associated with a flattening of the porphyrin ring. Alteration in the heme geometry causes weakening of the salt bridge between conserved Arg220 and heme propionate 7. Arg220 then moves into the heme binding

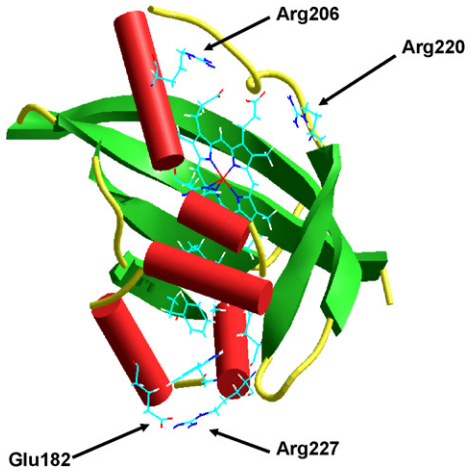


Fig. 15. Ribbon diagram of the FixL heme domain X-ray crystal structure in the ligand free-state (PDB entry 1XJ4). The heme cofactor is shown together with Arg206 and Arg220.

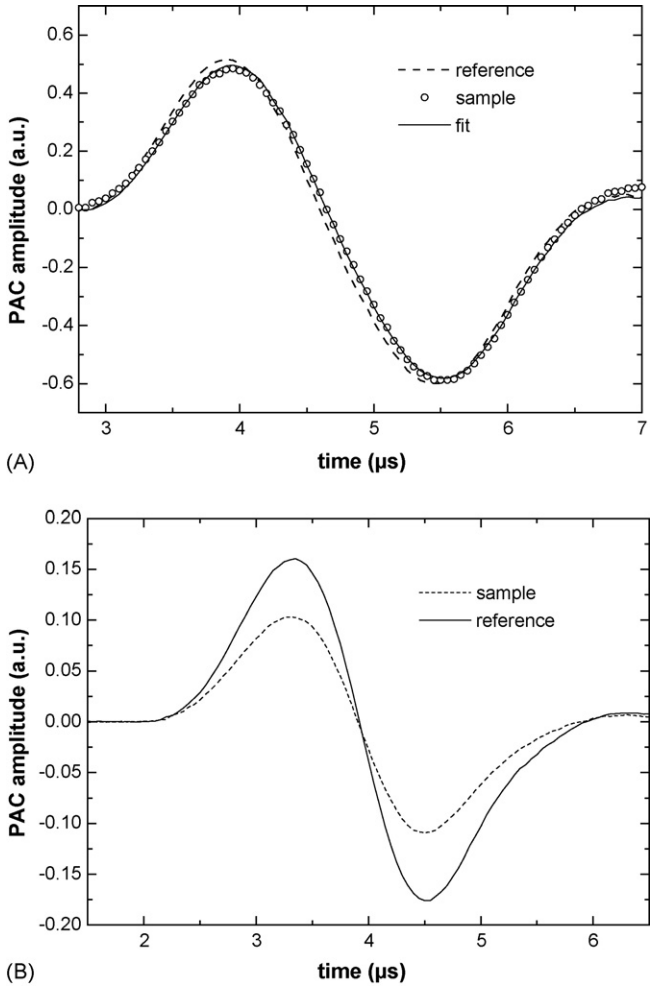


Fig. 16. Photoacoustic trace for CO photodissociation from CO *Bj*FixL$H_{140–270}$ (Panel A) and *Bj*FixL$H_{151–256}$ (Panel B) at 35 °C including corresponding reference traces. Conditions: 10 μM protein, 50 mM Tris buffer, pH 7.5, 50 mM NaCl and 1 mM CO.

pocket to form a hydrogen bond with the bound oxygen resulting in FG loop displacement whereas a second conserved Arg residue (Arg206) shifts to form a salt bridge with propionate 7 [95]. Albeit these structural changes are believed to represents the initial events of FixL signaling, the mechanism how changes within the heme binding pocket regulate the enzymatic activity of the kinase domain remains elusive [88].

To describe global conformational changes coupled to ligand dissociation from the FixL heme domain, we have determined volume and enthalpy changes associated with CO photo-dissociation from two heme domain constructs: a complete PAS heme domain, *Bj*FixL$H_{140–270}$, which begins with Thr170 and ends with Gln270; and a truncated heme domain, *Bj*FixL$H_{151–256}$. This construct has 11 residues deleted from the N-terminal end and 14 residues from the C-terminal end. Despite the fact that CO is not a physiological ligand for FixL and the crystal structure of CO bound FixL does not reveal significant conformational changes within the FG-loop, enzymatic studies have shown that CO binding to FixL results in appreciable inhibition of FixL enzymatic activity [99].

Photoacoustic traces for CO photodissociation from *Bj*FixL$H_{140–270}$ and the $Fe^{II}$4SP reference compound are shown in Fig. 16, Panel A. The sample trace is shifted in phase with respect to the reference trace indicating that CO dissociation occurs as a two-phase process. Deconvolution of the sample acoustic waves indicate a fast phase taking place faster than 50 ns and a subsequent phase occurring with the lifetime of 150 ns. From the temperature dependence of the amplitudes the volume and enthalpy changes corresponding to the fast and slow phases, were determined using Eq. (33) and a plot of $\phi_i E_{hv}$ versus $C_p\rho/\beta$ is shown in Fig. 17. To calculate the reaction volume and enthalpy changes, we used a $\Phi = 0.86$ previously determined by Rogers et al. [100] for *Sm*FixLH (although this value may be somewhat different for *Bj*FixLH). The fast phase is endothermic ($\Delta H = 14.0 \pm 3.0$ kcal mol$^{-1}$) and is characterized by a small volume contraction of $-1.4 \pm 0.8$ mL mol$^{-1}$. This phase is followed by a volume expansion of $5.3 \pm 0.7$ mL mol$^{-1}$ associated with an enthalpy change of $6.0 \pm 3.5$ kcal mol$^{-1}$. Contrary to these results, CO dissociation from truncated *Bj*FixL$H_{151–256}$ proceeds as a single step reaction occurring faster than 50 ns as judged from the absence of any phase shift between the sample and reference acoustic traces (Fig. 16, Panel B). The corresponding volume and enthalpy changes were determined from a plot of $\phi_i E_{hv}$ versus $C_p\rho/\beta$ (Fig. 17) and are $4.9 \pm 0.4$ mL mol$^{-1}$ and $25 \pm 4$ kcal mol$^{-1}$, respectively.

Interestingly the volume and enthalpy changes associated with the fast phase of CO dissociation from *Bj*FixL$H_{140–270}$ are similar to those determined for fast phase of CO dissociation from Mb as described in Section 4, suggesting that in both cases this phase may reflect similar molecular processes including Fe–CO bond cleavage, low-spin to high-spin heme transition with concomitant changes in heme geometry and possibly ligand movement within the heme binding site. In the case of myoglobin, the negative volume change has been attributed to the cleavage of a salt bridge between Lys45/Arg45 and heme propionate group [101,102]. An overlay of the CO bond *Bj*FixLH structure with the deoxy*Bj*FixLH structure does not reveal disruption of salt bridge between Arg220 and heme propionate group. However, Arg206 which is hydrogen bonded to the main chain carbonyl oxygen of Asp212 in the deoxy structure was shown to become disordered in the CO bound *Bj*FixLH structure [98]. An increase in solvent exposure and accompanying electrostriction could also account for observed volume decrease. Other structural changes which may be either transient or simply do not occur within the crystallized form of the protein may contribute to the observed PAC signal in the solution. Such changes are likely to include formation/cleavage of a surface exposed salt bridge between Glu182 and Arg227 which may, in turn, change

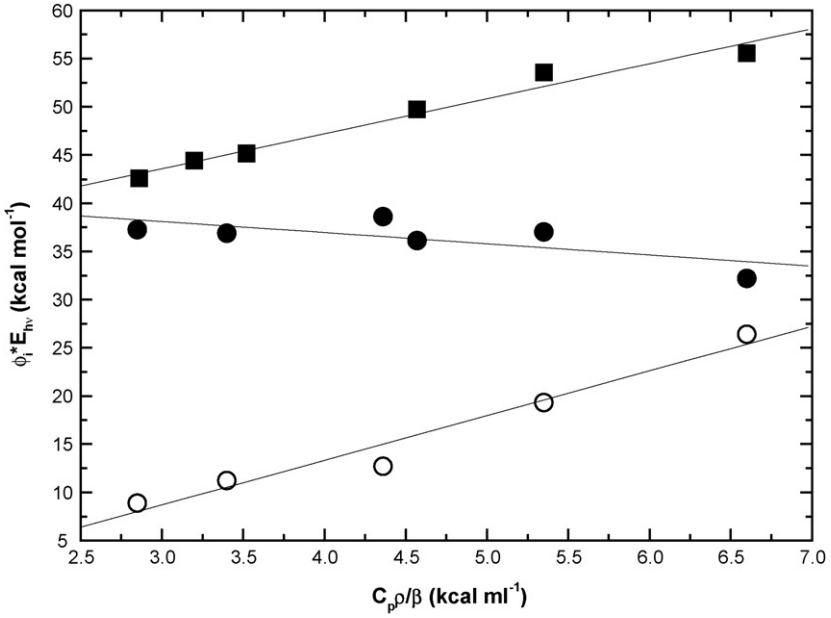


Fig. 17. Plot of $\phi_i E_{hv}$ vs. $C_p\rho/\beta$ for the fast phase (solid circle) and slow phase (open circle) of CO photodissociation from *Bj*FixL$H_{140–270}$ and for the single fast phase (solid square) from *Bj*FixL$H_{151–256}$.

the overall surface charge distribution. An analogous salt bridge was previously identified in the non-heme PAS protein, LOV, and proposed to play important role in interactions between the LOV domain and its interaction partner [101].

The initial contraction is followed by an endothermic ($\Delta H = 6.0 \pm 3.5$ kcal mol$^{-1}$) volume expansion ($\Delta V = 5.3 \pm 0.8$ mL mol$^{-1}$) occurring with a lifetime of 150 ns. We associate this process to ligand migration through the protein matrix or ligand escape to the surrounding solvent and concomitant protein conformational changes. The release of CO to the solvent is expected to be associated with positive volume change since the CO molar volume is ~35 mL mol$^{-1}$. The significantly smaller volume change determined for the 150 ns phase suggests that additional conformational changes are associated with ligand migration/release. Interestingly, the 150 ns kinetic phase has not been observed in previous studies using optical techniques [102], suggesting that this phase corresponds to structural changes that are distant from the heme binding pocket. On the other hand, CO dissociation from *Bj*FixL$H_{151–256}$ does not exhibit a comparable 150 ns phase although the values of volume and enthalpy changes detected within 50 ns are close to the sum of the volume/enthalpy changes measured for the fast and slow phases in *Bj*FixL$H_{140–270}$. Consequently, we consider that truncation of 11 amino-acid residues at the N-terminus and 14 amino acid residues at the C-terminus accelerate the release of the ligand from the protein. Our photoacoustic data suggest that conformational changes associated with ligand release from *Bj*FixLH are not localized in the vicinity of the heme binding pocket but extend outside of the heme pocket. Key and Moffat reported [98] that ligand binding to *Bj*FixLH induces changes in two $\beta$ sheets ($I_\beta$ and $G_\beta$) which propagate from the heme site towards the C-terminal helix linking the sensory domain to the kinase domain. These results suggest that conformational changes associated with signal propagation in FixLH are complex and are likely to be delocalized across a larger part of protein.

## 6. Thermodynamics of ligand/electron transfer in heme–copper oxidases

### 6.1. General background

Heme/copper oxidases form a diverse class of respiratory proteins found in nearly all aerobic organisms [103–107]. Although these enzymes range in molecular weight and subunit composition, several common features are found throughout the class. The majority of heme/copper oxidases contain at least three subunits (SU I, SU II, and SU III) with SU I containing the majority of the redox active metal centers (Fig. 18, top left) including two heme chromophores (heme *a*, heme *b*, and/or heme *o*) and at least one copper ion (Fig. 18, top right). One of the two hemes contains a heme iron that is six-coordinate and low spin which functions as a catalyst for electron transfer (ET) to the binuclear center. The binuclear center consists of the remaining heme (designated heme $a_3$, heme $o_3$, or heme $b_3$ depending upon the organism), which contains a five coordinate high spin heme iron and a copper ion (designated $Cu_B$). In addition, heme/copper oxidases from higher organisms contain an additional binuclear copper cluster (designated $Cu_A$) which accepts electrons from cytochrome *c*. All members of this class catalyze the four electron reduction of dioxygen to water and it is widely believed that most of these enzymes are energy transducing, i.e., they couple redox free energy to the active transport of protons across a membrane.

The overall reduction of dioxygen requires four protons to be consumed from the interior side of the membrane to form two water molecules. During the reduction reaction, four additional protons are vectorially translocated against a membrane potential from the interior to the exterior side of the membrane. Although the mechanism of active transport in heme/copper oxidases has not yet been fully elucidated, there is now clear experimental evidence that the ET steps within the catalytic cycle are well choreographed with proton uptake and release [108–113]. Studies using site directed mutants as well 3D structural models have now established two proton translocating channels that direct protons to the binuclear center [109,110]. The so-called K-channel begins with Lys319 proceeds through Thr316, Thr309, Ser255, Tyr244 and ends at the binuclear center (bovine heart numbering). The D-channel has an entryway on the cytoplasmic side formed by Asp91 and continues through Asn98 and comes into close proximity of the binuclear center through Glu242. It is believed that the K-channel is active during the first phase of the reaction cycle in which the enzyme accepts two electrons and takes up two protons whereas the D-channel conducts protons to the binuclear center as well as to periplasm during the reduction of various dioxygen intermediates.

Upon input of the first two electrons into the fully oxidized enzyme two protons are taken up from the matrix side of the membrane via the K-channel (Fig. 18, bottom) (O to R transitions). At this point, dioxygen binds to the heme $a_3$ group of the binuclear center resulting in heterolytic cleavage of the O–O bond via the transfer of four electrons to the bound oxygen (P-state): two electrons being derived from heme $a_3$ (forming a heme $a_3$ oxyferryl intermediate) one electron being derived from $Cu_B{}^{1+}$ and one electron from a tyrosine covalently linked to a histidine bound to $Cu_B$ (forming a tyrosine radical). Subsequent ET from heme *a* (reduced via ET from cytochrome *c* to $Cu_A$ and subsequent ET from $Cu_A$ to heme *a*) to the oxyferryl heme $a_3$ of the P-state results in reduction of the tyrosine radical and subsequent proton transfer from Glu242 to either the deprotonated tyrosine or a hydroxide bound to $Cu_B$ forming the F-state. Since each electron transferred to the binuclear center appears to be coupled to proton input, an additional proton is taken up during the P to F transition. In addition, at least one proton is also pumped across the membrane at this point in the catalytic cycle. Reduction of the F-state by subsequent ET from cytochrome *c* results in the formation of a hydroxide bound ferric heme $a_3$, the input of two protons and the pumping of one additional proton. There is now evidence that electron input from cytochrome *c* to the binuclear center to initiate a new turnover cycle (once the enzyme has completed a full turnover cycle) also results in the pumping of additional protons (O to R transition). The exact mechanism through which protons are actively translocated across the membrane barrier is not clear and a number of models have been proposed [105,111–113].

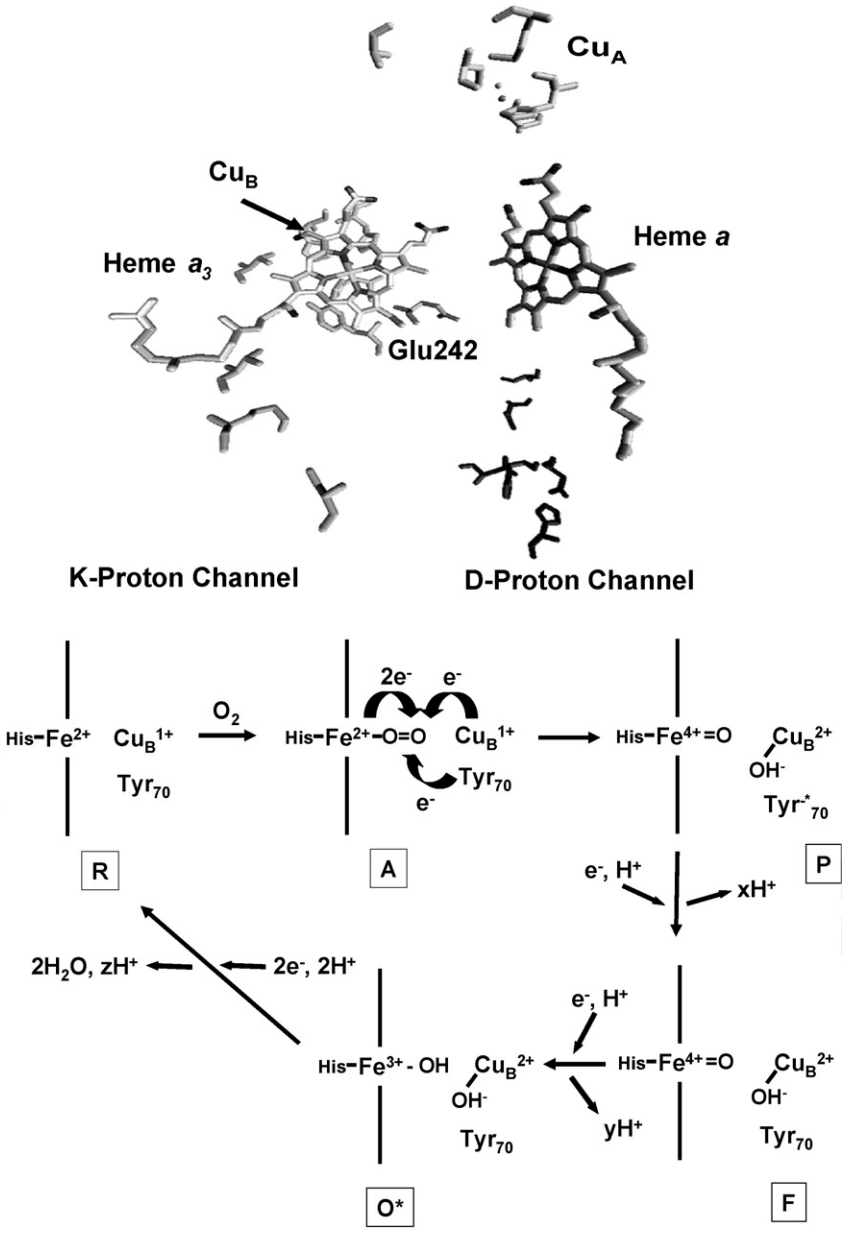


Fig. 18. Top metal center orientation within bovine heart CcO. Bottom: Proposed catalytic mechanism for CcO.

The most recent models involve electrostatic repulsion between protons within proton loading sites within the enzyme and protons imported from the input channels upon electron input. In any event, the transfer of electrons is intimately connected with the active transport of protons.

### 6.2. Ligand binding in fully reduced heme/copper oxidases

The binding of dioxygen to the binuclear center represents the initial step in the catalytic cycle. Carbon monoxide provides an extremely useful probe for examining the mechanistic details of ligand binding to a wide range of heme proteins due to the high quantum yield for photolysis and the reversibility of the reaction. In the case of heme/copper oxidases CO has been used to examine ligand binding to the fully reduced form of the enzyme as well as several mixed valence states [117–129]. These studies have revealed that, subsequent to photolysis of CO from heme $x_3$ CO binds transiently to $Cu_B$ within <1 ps and thermally dissociates from $Cu_B$ with a rate constant that is dependent on the nature of the enzyme (see Scheme 4). Cytochrome *c* oxidase

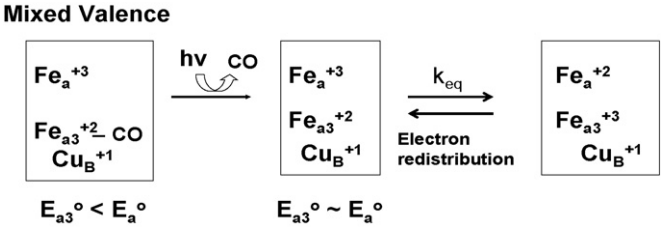


Scheme 4.

from bovine heart muscle exhibits a thermal dissociation rate constant of $\sim 7 \times 10^5\ s^{-1}$ [127], cytochrome $bo_3$ from *E. coli* (Cbo) of $\sim 500\ s^{-1}$ [102] and cytochrome $ba_3$ from *Thermus thermophylus* of $\sim 35\ s^{-1}$ [121].

CO-binding to fully reduced Cbo/CcO occurs on a ms timescale at room temperature (pseudo-first order rate constant of $\sim 100\ s^{-1}$ with 1 atm CO). The activation volumes and activation enthalpies used to construct the volume/enthalpy profiles were determined from Arrhenius plots (activation enthalpy, $\Delta H^{\ddagger}$, for CO binding of 3.13 kcal mol$^{-1}$ for Cbo as compared with 2.39 kcal mol$^{-1}$ for CcO [115]) and the pressure dependence of the CO recombination rate (activation volume, $\Delta V^{\ddagger}$, is found to be $13.3 \pm 2$ mL mol$^{-1}$ and $-9.0$ mL mol$^{-1}$ for Cbo and CcO, respectively) [38,40,123].

The total volume and enthalpy associated with CO dissociation from heme $a_3$ and subsequent binding to $Cu_B$ as well as the thermal dissociation of CO from $Cu_B$ to the bulk solvent have been determined using PAC. Analysis of the PAC data revealed two kinetic processes taking place subsequent to photolysis with the first occurring in <50 ns ($\Delta H = \pm 39$ kcal mol$^{-1}$; $\Delta V = \pm 7$ mL mol$^{-1}$) and a second process occurring with a lifetime of 1.5 μs ($\Delta H = -17$ kcal mol$^{-1}$; $\Delta V = \pm 7$ mL mol$^{-1}$) which are associated with Fe–CO bond cleavage and rapid transfer of CO to $Cu_B$ (<50 ns) and the thermal release of CO from $Cu_B$ which occurs with a lifetime of ~2 μs in bovine heart CcO. Previous studies have suggested that the enthalpy associated with Fe–CO bond cleavage is on the order of 17–20 kcal mol$^{-1}$ while the binding of CO to the $Cu_B$ site is estimated to be on the order of $-2$ kcal mol$^{-1}$ [48,123]. Thus, of the observed 39 kcal mol$^{-1}$, ~15 kcal mol$^{-1}$ can be attributed to ligand dissociation from the heme $a_3$ iron and subsequent CO–Cu bond formation. The origin of remaining ~24 kcal mol$^{-1}$ is not clear. One possibility is that binding of the CO to the $Cu_B$ site results in local structural reorganization of the $Cu_B$ coordination sphere and/or perturbations near the heme $a_3$ site subsequent to CO photodissociation. In fact, previous time-resolved FTIR studies have shown significant shifts in vibrational frequencies attributed to Cu–His bonding upon the transfer of CO from heme $a_3$ to $Cu_B$ in bovine heart CcO (Cu–His $\nu_{38}$, 1535 cm$^{-1}$ observed for the CO–$Cu_B$ complex but not observed in the CO–$Fe_{a3}$ species) occurring within the first 5 μs subsequent to photolysis [116].

The corresponding 1.5 μs phase corresponds to the thermal release of CO from $Cu_B$ and subsequent diffusion into the bulk solvent. As mentioned above the enthalpy for CO–$Cu_B$ bond formation is approximately $-2$ kcal mol$^{-1}$ while the enthalpy for solvation of CO due to entry of CO into the bulk solvent is on the order of approximately $-3$ kcal mol$^{-1}$. Thus, in the absence of any conformational change associated with CO release would be approximately $-1$ to 2 kcal mol$^{-1}$. The corresponding volume is estimated to be $\pm 15$ mL mol$^{-1}$ (approximately $\pm 5$ mL mol$^{-1}$ for metal–ligand bond cleavage and approximately +20 mL mol$^{-1}$ for CO solvation [123]). These values suggest that a significant conformational change accompanies CO release from $Cu_B$ with $\Delta H_{conf} = \Delta H_{obs} - \Delta H_{estimated} = -32$ kcal mol$^{-1}$ and $\Delta V_{conf} = \Delta V_{obs} - \Delta V_{estimated} = -8$ mL mol$^{-1}$. Such a conformational change possibly places the binuclear center into a 'ligand accepting' state which would be associated with oxygen binding.

In contrast to bovine heart CcO, the PAC signals for the CO–Cbo overlay in time with those of the reference compound indicating that all volume/enthalpy changes occur on a timescale faster than the detector response time (i.e., <50 ns). A plot $\phi E_{h\nu}$ (kcal mol$^{-1}$) versus $C_p\rho/\beta$ (kcal mL$^{-1}$) gives a $\Delta H$ of $\pm 23 \pm 7$ kcal mol$^{-1}$ and an accompanying volume decrease of $5.1 \pm 0.9$ mL mol$^{-1}$ (for CO photolysis) [38]. The lack of a slow phase is consistent with the fact that the rate of thermal CO release from $Cu_B$ is an order of magnitude slower than for bovine heart CcO and is therefore outside the detection range of our PAC detector. However, the <50 ns $\Delta H/\Delta V$ values are quite distinct between Cbo and bovine heart CcO although in both enzymes, CO photolysis results in Fe–CO bond cleavage, low-spin to high-spin transition at the heme $x_3$ site and CO binding to $Cu_B$. The observed enthalpy change is roughly 12 kcal mol$^{-1}$ lower for Cbo while the volume change is 12 mL mol$^{-1}$ lower. This suggests that perturbations to the $Cu_B$ site upon ligand transfer are quite distinct between the bacterial and mammalian enzymes. In fact, previous EXAFS studies of Cbo have suggested that CO dissociation from heme $o_3$ and its rebinding to $Cu_B$ leads to an increase of the bond length between the copper and two histidine ligands which may contribute to the observed volume/enthalpy change [123,125]. In addition, FTIR studies have shown that CO transfer to $Cu_B$ results in perturbations to Glu286 which is located at the end of the D-channel for proton input [114,115]. Overall these results suggest that CO transfer to $Cu_B$ induces a structural change within the binuclear center that is distinct from that observed in the mammalian enzyme.

In contrast to bovine heart CcO and *E. coli* Cbo, phototodissociation of the fully reduced carbonmonoxy bound cytochrome $aa_3$ from *Rb. sphaeroides* results in ultrafast ligand transfer between heme $a_3$ and $Cu_B$, which is followed by thermal dissociation from $Cu_B$ on longer time scales as well as an additional process, which has not been characterized previously, with a lifetime of 485 ns at 18 °C. This process is coupled to a volume expansion of 3.3 mL mol$^{-1}$. From the temperature dependence, an activation barrier of 4 kcal mol$^{-1}$ was determined (see Fig. 19 for a summary). The enthalpy changes occurring in <50 ns subsequent to CO photolysis from RbCcO is close to that previously determined for CO photodissociation from Cbo heme $o_3$ (23 kcal mol$^{-1}$) and bovine heart CcO heme $a_3$ (~39 kcal mol$^{-1}$) (analysis of $Q_{a3}$ from Ref. [40]). Interestingly, no volume change is observed indicating that this process in purely enthalpy driven in RbCcO.

The ~500 ns phase of CO RbCcO photolysis is characterized by an expansion of ~3 mL mol$^{-1}$ and a negligible change in enthalpy. Interestingly, this phase has not been observed in time resolved absorbance measurements indicating that the changes corresponding to this event do not lead to perturbations of the heme electronic structure. From the Arrhenius plot the activation energy for this phase is found to be $4.1 \pm 0.9$ kcal mol$^{-1}$. The absence of any significant enthalpy change indicates that the volume expansion is mainly entropy driven. Although the

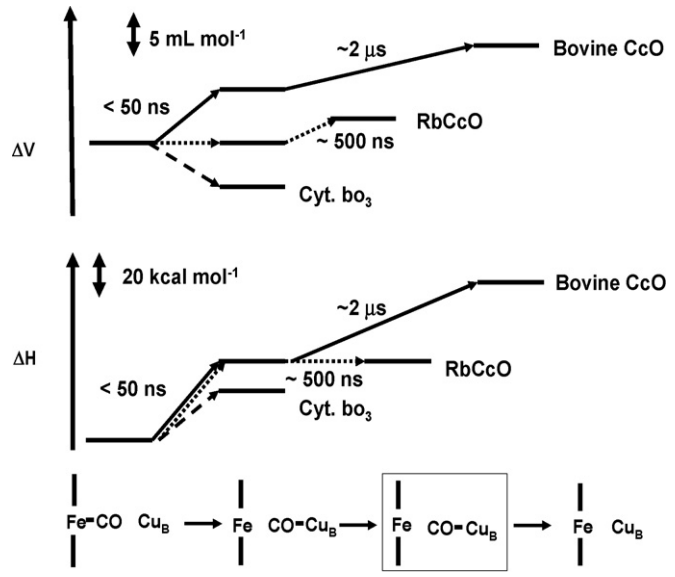


Fig. 19. Thermodynamic profiles for the photolysis of CO from the fully reduced CO bound forms of bovine heart CcO (solid lines), *E. coli* cytochrome $bo_3$ (dashed lines) and Rb CcO (dotted lines). The 'boxed' species represents the 500 ns transient, only observed for CORbCcO photolysis.

precise origin of this phase is unclear it is likely that this phase involves a relaxation following CO binding to $Cu_B$ or both.

As already mentioned, upon dissociation from heme $a_3$ CO binds transiently to $Cu_B^{1+}$ prior to diffusion out of the active site. Interestingly, thermal dissociation of CO from $Cu_B$ does not result in CO rebinding to heme $a_3$ which might be expected due to the close proximity of the two metal centers (4.6 Å). Thus, CO binding to $Cu_B$ must trigger a conformational rearrangement at the $Cu_B$/heme $a_3$ site that significantly increases the energy barrier for heme $a_3$ ligand binding while lowering the barrier for CO diffusion out of the active site pocket. With this in mind it is important to point out that previous EXAFS studies of Cbo have suggested that CO dissociation from heme $o_3$ and subsequent binding to $Cu_B$ leads to an increase of the bond length between the copper and two histidine ligands [125]. The fact that the 500 ns process only involves a change in volume (i.e., no enthalpic component) is consistent with this type of rearrangement rather than $Cu_B$–His bond dissociation. At this point it is not clear how such a rearrangement would affect the barrier for CO recombination to heme $a_3$.

It is of interest to note that the <50 ns processes in bovine heart CcO and the combined <50 ns and ~500 ns events in RbCcO are similar with $\Delta H \sim 35$ kcal mol$^{-1}$ and $\Delta V \sim \pm 5$ mL mol$^{-1}$ suggesting that conformational perturbations to the $Cu_B$ site upon CO transfer from heme $a_3$ are similar for the two enzymes but occur on different timescales. This is in clear contrast to Cbo exhibits distinct dynamics upon CO binding to $Cu_B$. Since both bovine heart CcO and RbCcO display similar thermodynamics subsequent to CO transfer to $Cu_B$ it is unlikely that these dynamics involve Glu (I-286) perturbations suggesting that this event must take place on a time scale between ~50 ns and ~2 μs at which time thermal dissociation of CO from the $Cu_B$ site takes place in the bovine enzyme.

### 6.3. Mixed valence heme/copper oxidases

A very useful method to probe the relationship between proton transport and intramolecular ET in heme/copper oxidases involves photolysis of the CO mixed valence derivative of the enzyme [126–129]. In this state, CO is bound to ferrous heme $x_3$ (where $x = a$, $b$, or $o$ depending upon the species) and the $Cu_B$ ion is in the +1 state. The remaining metals remain oxidized (heme $x$/$Cu_A$ for cytochrome oxidases, heme $x$ for quinol oxidases). Photolysis of the CO from the heme $x_3$ site results in a lowering of the heme $x_3$ reduction potential allowing for rapid ET between the ferrous heme $x_3$ and ferric heme $x$ (Scheme 4). In CcO subsequent ET takes place between heme $x$ and the cupric $Cu_A$ site. The rates of intramolecular ET depend upon the nature of the species from which the enzyme was isolated. Photolysis of CO mixed valence CcO from bovine heart muscle (COMVCcO) results in rapid transfer of CO from heme $a_3$ to $Cu_B$ (~ps) followed by rapid ET from heme $a_3$ to heme $a$ (1.2 ns) [131]. Further heme $a_3$ to heme $a$ ET occurs on a ~3 μs timescale and it is believed that this ET event is coupled to the thermal release of CO from $Cu_B$ since the CO dissociation rate is also ~3 μs in the fully reduced enzyme where heme $a_3$ to heme $a$ ET does not occur. Additional ET between heme $a$ and $Cu_A$ occurs on a much longer timescale (~75 μs).

Previous FTIR results of the photostationary state of the COMVCcO have demonstrated pH dependent perturbations [132,133]. It was shown that the photostationary state results in perturbations to Glu242 (attributed to deprotonation of this residue), redox induced shifts in heme propionate vibrational frequencies and redox linked protonation of an Arg residue which appears to accompany ET between heme $a_3$ and heme $a$. These studies could not resolve which ET event was associated with the proton transfer events (i.e., the ns fast phase or the slower phase coupled to thermal release of CO from $Cu_B$). What is of specific interest is the fact that the protonation state of Glu242 which is located at the end of the D-channel and donates protons to the binuclear center during the P to F transition is directly linked to the redox state of heme $a$/heme $a_3$.

The obvious relationship between the energetics of ET and the active transport of protons necessitates a complete understanding of the thermodynamics associated with various ET reactions within the enzyme as well as their pH dependence. Fig. 20 displays an overlay of the acoustic traces for COMVCcO and the calorimetric reference obtained at pH 6, 8, and 9 [130]. The acoustic waves obtained at both pH 6 and 8 for CO photolysis from the COMVCcO show significant phase shifts relative to those of the corresponding reference compounds. From deconvolution of the sample acoustic waves three kinetic events can be resolved (Fig. 21). The first occurs faster than the time resolution of the instrument (i.e., $\lesssim$50 ns), the second has a lifetime of ~100 ns and the third occurs with a lifetime of ~2 μs (at 20 °C). Analysis of the temperature dependence of the deconvoluted acoustic amplitudes at pH 6 gives volume and enthalpies associated with the three kinetic phases: $\Delta H_1/\Delta V_1 = +79 \pm 10$ kcal mol$^{-1}$/$+9 \pm 1$ mL mol$^{-1}$; $\Delta H_2/\Delta V_2 = -79 \pm 5$ kcal mol$^{-1}$/$-9 \pm 2$ mL mol$^{-1}$; $\Delta H_3/\Delta V_3 = +54 \pm 7$ kcal mol$^{-1}$/$+8 \pm 1$ mL mol$^{-1}$ (Fig. 22). Similar

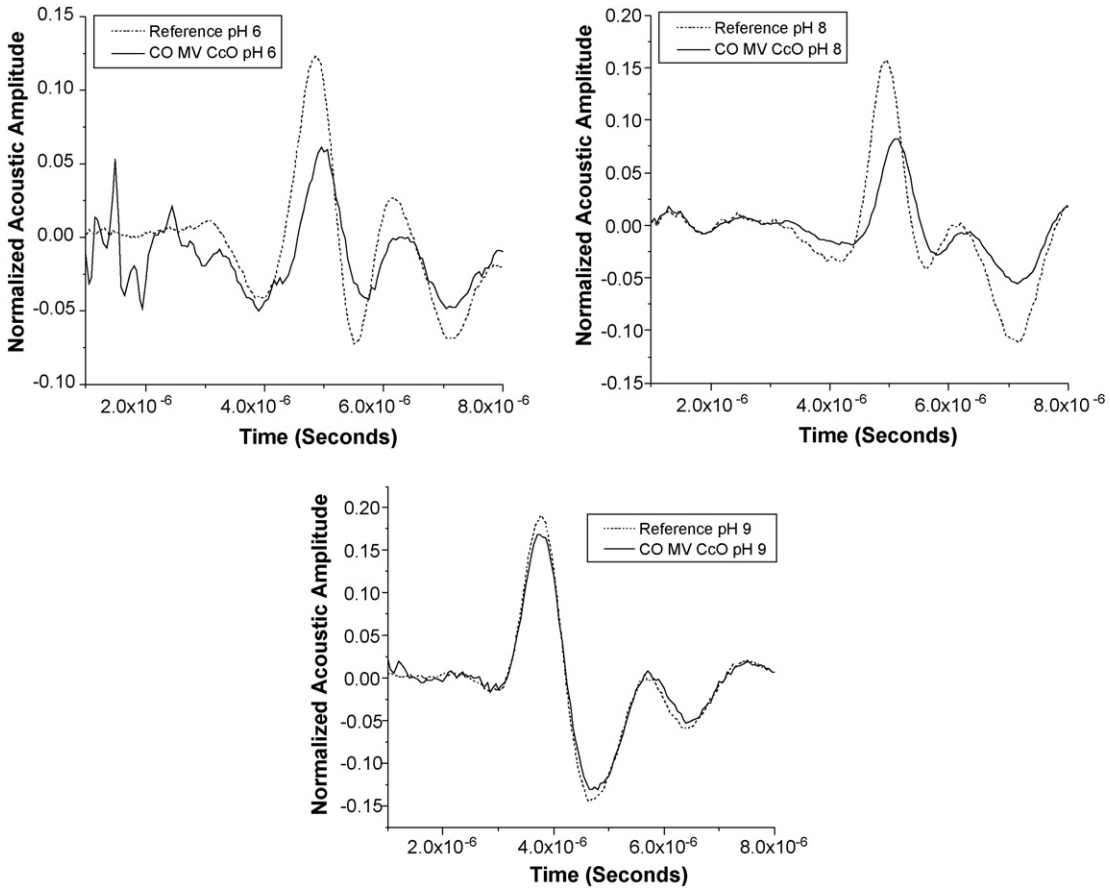


Fig. 20. Overlay of COMVCcO and calorimetric reference acoustic signals obtained at pH 6 (top left), pH 8 (top right) and pH 9 (bottom). Sample conditions: [CcO] = 16 μM in 50 mM HEPES buffer containing 0.05% β-D-laurylmaltoside.

volume and enthalpy changes are observed at pH 8. Interestingly, no phase shift is observed at pH 9. Analysis of the amplitudes of the sample and reference acoustic waves obtained at pH 9 reveal no significant volume change (i.e., $\Delta V \sim 0$) and a $\Delta H$ of +29 kcal mol$^{-1}$. The thermodynamic profiles are summarized in Fig. 23.

The fact that the thermodynamic parameters for processes occurring in <50 ns associated with CO photolysis from the COMVCcO are distinct from those obtained for the fully reduced form of the enzyme suggest that additional processes take place in the COMV form of the enzyme. In both the COMV and fully reduced forms of CcO, CO photolysis results in the rupture of the Fe–CO bond, low-spin to high-spin transition and CO–$Cu_B$ formation. In the case of the COMV form, it has been shown that fast ET takes place with a lifetime of ∼1.2 ns [131]. Thus, the total volume and enthalpy changes for the COMVCcO contain additional parameters associated with the ET between heme $a_3$ and heme $a$. The thermodynamic events associated with the fast ET can be directly obtained using the parameters obtained from the fully reduced enzyme. The average thermodynamic parameters associated with heme $a_3$ to heme $a$ ET at pHs below 9 are: $\Delta H_{ET}^{COMV} = +40$ kcal mol$^{-1}$ and $\Delta V_{ET}^{COMV} = +2$ mL mol$^{-1}$. These thermodynamic parameters are nearly equivalent between pH 6 and 8. Previous studies have suggested that the ultra-fast ET (occurring on the 1.2 ns time scale) accounts for only ∼16% of the total heme $a_3$ to heme $a$ ET [131]. Scaling $\Delta H_{ET}^{COMV} = +40$ kcal mol$^{-1}$ and $\Delta V_{ET}^{COMV} = +2$ mL mol$^{-1}$ to the ET yield gives 250 kcal mol$^{-1}$ and 12.5 mL mol$^{-1}$ for the reaction. The magnitude of the enthalpy value suggests that additional conformational processes must occur in the COMV form of the enzyme, possibly accompanying the ultra-fast ET, which would contribute to the $\Delta H_{ET}^{COMV}$ term (i.e., $\Delta H_{ET}^{COMV} = \Delta H_{ET\text{-effective}}^{COMV} + \Delta H_{conf}^{COMV}$). Estimates of the values of these enthalpies can be made using the ∼2 μs data discussed below. What is notable is that the PAC results indicate both fast ET as well as a corresponding reorganization of the heme $a_3$/$Cu_B$ active site that may be coupled to the ET reaction.

In fully reduced COCcO photolysis results in the rapid transfer of CO from heme $a_3$ to $Cu_B$ within a few picoseconds. Subsequent thermal dissociation of CO from the $Cu_B$ site occurs with a lifetime of ∼1.7 μs as discussed previously. In the case of the COMVCcO previous results have also suggested that intra-molecular ET also occurs between heme $a_3$ and heme $a$ that is coupled to CO release from $Cu_B^{1+}$ [126–128,130,132], The slow phase kinetics observed subsequent to photolysis of the COMVCcO presumably contains thermodynamic parameters for both the thermal dissociation of CO as well as any intra-molecular ET between the two hemes. Assuming that the $Cu_B^{1+}$–CO bond energy is the same in both the COMV and

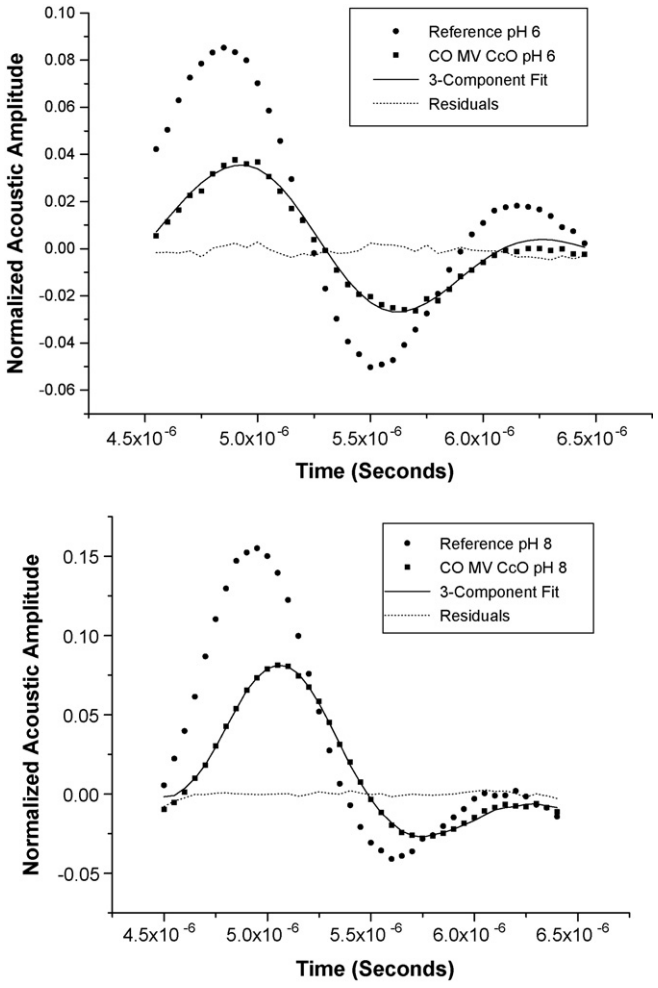


Fig. 21. Deconvolution of the acoustic waves for COMVCcO obtained at various pHs. Plots show an overlay of acoustic waves for COMVCcO, calorimetric reference, three-exponential fit and residuals. Top panel: fits for pH 6; bottom panel: fits for pH 8.

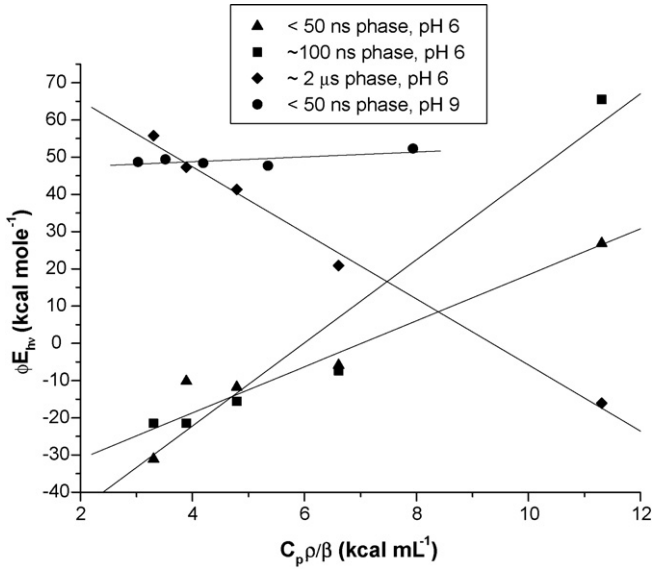


Fig. 22. Plot of $\phi E_{h\nu}$ vs. $C_p\rho/\beta$ or the acoustic signals obtained at pH extremes, pH 6 and 9. The normalized amplitudes ($\phi_i$) for the various phases at pH 6 were obtained from the deconvolution of the acoustic waves as per Fig. 21.

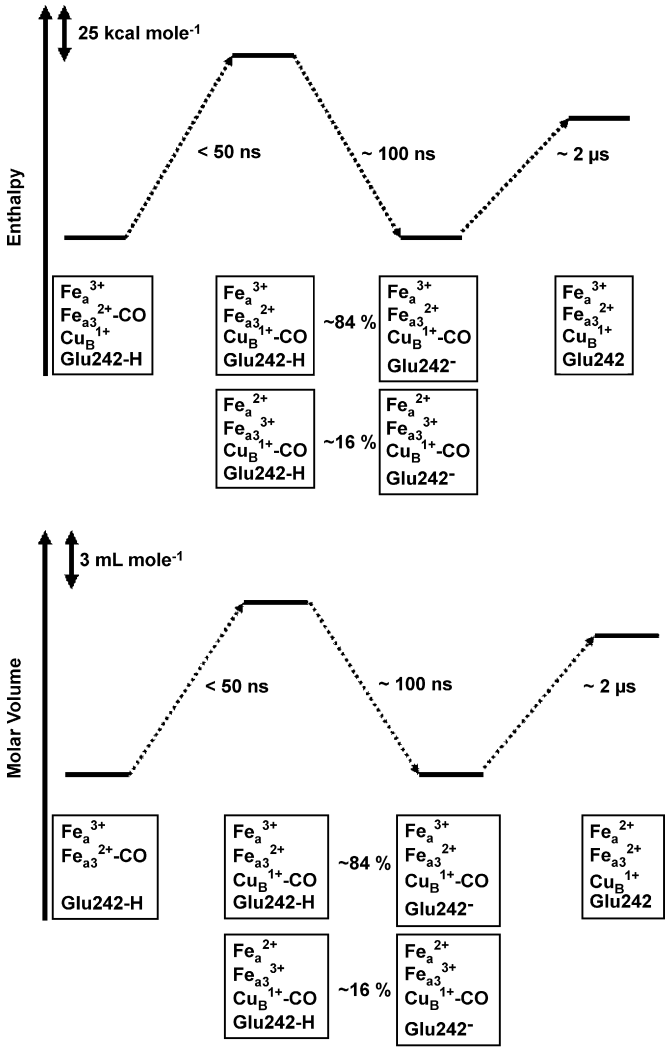


Fig. 23. Thermodynamic profiles (molar volume and enthalpy) for photolysis of COMVCcO at pHs < 9.

fully reduced forms of the enzyme then the thermodynamic parameters associated with intramolecular ET can also be calculated [130]. At pHs below 9 the thermodynamic parameters are: $\Delta H_{ET}^{COMV} \sim 20\,kcal\,mol^{-1}$ and $\Delta V_{ET}^{COMV} \sim 1\,mL\,mol^{-1}$. This also assumes that $\Delta H_{Conf}$ and $\Delta V_{Conf}$ are also equivalent between the COMVCcO and CO–CcO. If the observed $\Delta H_{ET}^{COMV}$ is 20 kcal mol$^{-1}$ and this enthalpy represents 86% of the total ET then the actual enthalpy change for the ET reaction ($\Delta H_{ET}^{COMV}$) is +23 kcal mol$^{-1}$. Using this value gives $\Delta H_{ET\text{-}conf}^{COMV}$ observed in the fast phase to be +36 kcal mol$^{-1}$. The 0.16 scaling factor is used since only 16% of the total ET occurs in the fast phase. The observed volume change is also quite small for the ET reaction which is consistent with no additional conformational change taking place. The ET reaction itself results in no net change in charge ($Fe_a^{3+}$ $Fe_{a3}^{2+}$ –>$Fe_a^{2+}$ $Fe_{a3}^{3+}$) therefore no electrostriction would occur and $\Delta V$ would be negligible.

The origin of the ~100 ns phase is not clear. It is not observed in the fully reduced form of the enzyme nor has such a phase been identified in previous transient absorption studies on this time scale. One hypothesis is that the ~100 ns phase represents

either a change in the protonation state of Glu242 or a conformational perturbation to this residue or both. Previous FTIR studies of the mixed valence form of bovine CcO have shown that reverse ET from heme $a_3$ to heme $a$ is accompanied by deprotonation of Glu242. This is evident by the appearance of a trough at 1735 $cm^{-1}$ in the photolyzed minus unphotolyzed CO mixed valence difference spectrum (arising from Glu242 $\nu_{C=O}$) [116,125]. A corresponding carboxylate peak is also observed at 1412 $cm^{-1}$. The nature of the subsequent proton acceptor has not been identified but a putative mechanism involves protonation of an Arg residue near the near the formyl group of heme $a$. The same FTIR studies have revealed vibrational stretches consistent with protonation of a neutral Arg (vibrational features at 1638/1676 $cm^{-1}$ in the photolyzed/unphotolyzed COMV difference spectrum). The Arg residues near the heme propionates (Arg438 and Arg439) have been ruled out since these residues are located in a hydrophilic region of the protein making it unlikely that any significant population of the deprotonated state would exists. An alternative assignment involves protonation of Arg38 which forms a hydrogen bond with the formyl group of heme $a$ since Arg38 is in a more hydrophobic region of the binuclear center.

The thermodynamics associated with this phase ($\Delta H_2/\Delta V_2 = -79 \pm 5$ kcal $mol^{-1}/-9 \pm 2$ mL $mol^{-1}$) are consistent with deprotonation. The observed volume contraction could result from significant electrostriction produced within the enzyme by the redistribution of charge (i.e., deprotonation of Glu242 and protonation of the neutral Arg38). In fact, charge separation in bacterial photosynthetic reaction centers from *Rb. sphaeroides* as well as photosystem I (PSI) from *Synechocystis* exhibit volume contractions on the order of −9 to −16 mL $mol^{-1}$ upon charge transfer (i.e., $P_{870}{}^{+}Q_A{}^{-}$ formation in bacterial reaction centers and $P_{700}{}^{+}F_{AB}{}^{-}$ formation in PSI) [134]. Typical values for electrostriction for charge formation in water are in the −15 mL $mol^{-1}$ and the lower value in CcO may reflect a lower dielectric constant within the binuclear center. The enthalpy for proton transfer is more difficult to interpret. Previous studies of the photocycle of bacteriorhodopsin have revealed that proton transfer from Asp96 to the retinal Schiff base ($M_2$ to N transition) has an associated change in enthalpy of only approximately −5 kcal $mol^{-1}$ whereas the N to O, which involves proton transfer from Asp85 to the 'release' group near the surface of the protein has an associated enthalpy change of approximately −20 kcal $mol^{-1}$ [135,136]. These enthalpies are considerably higher than the approximately −80 kcal $mol^{-1}$ observed for the 100 ns phase in the COMVCcO. It should be kept in mind that the enthalpy changes observed for proton transfer reactions in the bacteriorhodopsin photocycle also involve significant conformational changes which are also included in the enthalpy changes. Thus, the intrinsic proton transfer enthalpies cannot be isolated from the total enthalpy changes. In the case of CcO it is possible that the larger enthalpy values may represent only the proton transfer event. In fact, gas phase proton transfer reactions exhibit enthalpy changes which are much closer to the CcO values [137].

The assignment of the ∼100 ns phase to a proton transfer from Glu242 to Arg38 is supported, to some extent, by the fact that this phase is not present at pHs above 9 in which the Glu242 is likely to be deprotonated. It is also of interest that the μs phase is also absent at higher solution pH values. The pH dependence of this phase suggests that both thermal dissociation of CO from the $Cu_B{}^{1+}$ site and corresponding ET from heme $a_3$ to heme $a$ may be influenced by the protonation state of Glu242 indicating that the thermodynamics of thermally activated CO dissociation from $Cu_B{}^{1+}$ are coupled to the protonation state of Glu242. Thus, Glu242 may play a role in the modulation of the $Cu_B$ ligand environment.

We have also examined the volume and enthalpy changes accompanying CO photodissociation from the mixed valence form of Cbo [50]. An overlay of the sample and reference acoustic waves reveals a phase shift in the sample acoustic wave similar to the low pH acoustic waves of bovine heart CcO. Deconvolution of the acoustic waves reveals two decay processes, the first occurring with a lifetime shorter than the detection limit of our instrument (<50 ns) and a second has a lifetime of ∼250 ns at 18 °C. The first process shows a small contraction of $-1.3 \pm 0.3$ mL $mol^{-1}$ and an enthalpy of $32 \pm 1.6$ kcal $mol^{-1}$. The 250 ns process is characterized by a positive volume change of $2.9 \pm 0.5$ mL $mol^{-1}$ and an enthalpy change of $-5 \pm 3$ kcal $mol^{-1}$. The enthalpy changes for CO dissociation from heme $o_3$ is calculated as described in reference [50]. As with bovine heart CcO, subsequent to photolysis of CO from heme $o_3$ CO binds transiently to $Cu_B$ within <1 ps and thermally dissociates from $Cu_B$ with a rate constant of $8 \times 10^3$ $s^{-1}$ [114]. In the mixed valence form of the enzyme photolysis of CO is followed by electron equilibration between heme $o_3$ and heme $b$ which does not occur in the fully reduced enzyme. The back electron transfer between heme $o_3$ and heme $b$ occurs with a rate constant of $2 \times 10^5$ $s^{-1}$ which is too slow to be resolved by our PAC instrument. CO photo-dissociation from the fully reduced enzyme results in a negative volume change of approximately −5.1 mL $mol^{-1}$ occurring faster than 50 ns time resolution of the instrument suggesting that protein conformational changes accompany the ligand transfer between heme $o_3$ and $Cu_B$. In the case of the MV form of Cbo the volume decrease associated with the fast phase is ∼4 mL $mol^{-1}$ smaller than volume changes measured for the fully reduced enzyme. This indicates that structural changes, which are coupled to the CO transfer from heme $o_3$ to $Cu_B$, are affected by the oxidation state of heme $b$. The observed enthalpy change associated with the fast phase ($\Delta H = +32 \pm 2$ kcal $mol^{-1}$) is significantly higher than the enthalpy of CO dissociation from heme containing a nitrogenous base at the fifth coordination site ($\Delta H = 17$ kcal $mol^{-1}$) further suggesting the presence of structural changes associated with ligand transfer between the heme $o_3$ and $Cu_B$. To date there is no evidence of the ultra-fast ET between heme $o_3$ and heme $b$ that has been observed between heme $a_3$ and heme $a$ in bovine heart CcO. Thus, the 250 ns phase observed in the MV form of Cbo is likely due to conformational perturbations.

Overall, the results presented in this section demonstrate the diversity of conformational dynamics observed for ligand binding to heme/copper oxidases despite considerable structural homology among the enzymes in this class. It is also not clear if the differences in ligand binding dynamics are in any

way related to differences in proton pump mechanism between oxidases from different species. This remains an active area of investigation.

### 6.4. Conclusions and future prospects

The results presented here represent a survey of photothermal studies of heme–ligand interactions for various heme protein systems that have been examined in our laboratory. These studies illustrate the utility of photothermal methods in obtaining time-resolved thermodynamic profiles (both molar volume and enthalpy) for fast ligand dissociation reactions as well as the subsequent rebinding. Both photoacoustic calorimtery and photothermal beam deflection provide robust methods for obtaining not only molar volume and enthalpy changes for photoinitiated processes but also the rates at which these processes occur over a wide range of time (∼ns to 100 ms).

Although the ability to probe global conformational/thermodynamic changes associated with photo-triggered reactions is one advantage enjoyed by photothermal methods this also represents a significant limitation in that the observed changes can not necessarily be assigned to the movement of specific amino acid residues or even protein domains. These limitations can be overcome to some extent through the use of site-directed mutagenesis and/or different protein constructs. We have been working to overcome these limitations by coupling the time-resolved thermodynamic measurements with NPT molecular dynamics. Extended ensemble molecular dynamics (EEMD) is capable of providing an atomistically detailed description of molecular motions on time scales compatible with photothermal techniques while tracking any associated volume changes, and thus provides an ideal complement to such experiments. We have now tested this methodology using PAC synergistically combined with EEMD to determine the molecular volume change associated with the photoisomerization of aqueous *trans*-AB to *cis*-AB [138]. The NPT EEMD exactly samples both the NPT ensemble and the associated fluctuations in the pressure and temperature variables giving desired average values. The resulting dynamics is only slightly perturbed from true Newtonian motion and is sufficiently accurate to follow the time evolution of the system. During the simulation the volume coordinate fluctuates over time and the average value is the system volume. For non-equilibrium simulations, e.g., following protein folding dynamics, signaling events in gas sensing heme proteins, etc. this method of molecular volume determination can resolve time dependent volumes and, given the inherent precision, identify intermediates that have lifetimes on the order of nanoseconds. We are continuing to explore this methodology on larger protein systems and the results are very promising.

Rapid advances in the synthesis of so-called 'caged' molecules (i.e., bioactive molecules containing photo-cleavable protecting groups) offers a great opportunity to probe the conformational/thermo-dynamics of a much wider range of biological processes including cell signaling, ion-transport, pH sensitive process (e.g., protein folding), etc. [139]. These systems are particularly attractive for use with photothermal methods since release of the caged molecule occurs within the laser pulse and does not interfere with longer time thermodynamic processes associated with the protein/enzyme system being investigated. An alternative method for rapidly initiating biological processes is the laser temperature jump [140,141]. These experiments involve excitation of one of the normal vibrational modes of water (via a fast laser pulse) resulting in a temperature change of up to ∼10 K. Subsequent conformational dynamics associated with a given protein/enzyme can then be probed using fluorescence, resonance/normal Raman, IR, CD, MCD or other optical probe. Unfortunately, the laser temperature jump method is not amenable to use with either PAC or PBD since the magnitude of acoustic wave/refractive index change is sufficiently large due to the primary T-jump that the smaller acoustic waves/refractive index changes associated with the biological processes being investigated can not be resolved.

In terms of methodology, recent advances in transient grating spectroscopy, which is a photothermal method that probes the breakdown of a transiently induced density grating produced by constructive/destructive interference of two coincident laser pulses within a sample of absorbers provides dramatically improved time-resolution [142,143]. In addition, this technique can readily identify diffusion coefficients as well as other fast thermal processes on time scales down to hundreds of picoseconds. This technique has now been applied to several protein systems with great success.

Overall, photothermal methods have enjoyed success in probing the energetics and conformational dynamics of a wide range of biological systems. As these techniques continue to evolve in time resolution and sensitivity as well as the ability to couple photothermal measurements to MD simulations more detailed relationships will be developed between the change in molecular conformation and the energetics that control these processes.

## Acknowledgements

The Authors would like to acknowledge all of the current and former students who have participated in these projects over the years. Their contributions have been invaluable. The Authors are also indebted to the American Heart Association, National Science Foundation and Petroleum Research Fund for support of this work.

## References

[1] K.M. Smith (Ed.), Porphyrins and Metalloporphyrins, Elsevier, Amsterdam, 1975, p. 1.
[2] D. Dolphin (Ed.), The Porphyrins, Academic Press, New York, 1979.
[3] A.P.B. Lever, H.B. Gray (Eds.), Iron Porphyrins, Addison Wesley, Reading, Mass, 1989.
[4] M. Merchan, E. Orti, B. Roos, Chem. Phys. Lett. 226 (1994) 27.
[5] M. Gouterman, J. Mol. Spec. 6 (1961) 138.
[6] J.A. Shelnutt, V. Ortiz, J. Phys. Chem. 89 (1985) 4733.
[7] E. Antonini, L. Rossi-Bernardi, E. Chiancone (Eds.), Methods Enzymol, Vol. 76. Hemoglobins (Part A), Academic Press, San Diego, 1981.
[8] G.W. Pettigrew, G.R. Moore, Cytochromes *c* Biological Aspects, Springer–Verlag, Berlin/Heidelberg/New York, 1987.
[9] A.T. Smith, N.C. Veitch, Curr. Opin. Chem. Biol. 2 (1998) 269.
[10] B. Taylor, I.B. Zhulin, Microbiol. Mol. Biol. Rev. 63 (1999) 479.

[11] R.A. Goldbeck, D.B. Kim-Shapiro, D.S. Kliger, Ann. Rev. Phys. Chem. 48 (1997) 453.
[12] R. Schweitzer-Stenner, J. Raman Spec. 36 (2005) 276.
[13] S.E. Plunkett, J.L. Chao, T.J. Tague, R.A. Palmer, Appl. Spect. 49 (1995) 702.
[14] M. Bennati, T.F. Prisner, Rep. Prog. Phys. 68 (2005) 411.
[15] R.M. Esquerra, R.A. Goldbeck, S.H. Reaney, A.M. Batchelder, Y. Wen, J.W. Lewis, D.S. Kliger, Biophys. J. 78 (2000) 3227.
[16] R.A. Goldbeck, S.J. Paquette, D.S. Kliger, Biophys. J. 81 (2001) 2919.
[17] J. Hofrichter, J.H. Sommer, E.R. Henry, W.A. Eaton, Proc. Natl. Acad. Sci. U.S.A. 80 (1983) 2235.
[18] A. Bellelli, M. Brunori, Meth. Enzymol. 232 (1994) 56.
[19] B.A. Springer, S.G. Sligar, J.S. Olson, G.N. Phillips, Chem. Rev. 94 (1994) 699.
[20] Q.H. Gibson, L. Milnes, Biochem. J. 91 (1964) 161.
[21] M.I. Verkhovsky, N. Belevich, J.E. Morgan, M. Wikstrom, Biochim. Biophys. Acta 1412 (1999) 184.
[22] O. Einarsdottir, Biochim. Biophys. Acta 1229 (1995) 129.
[23] H. Michel, J. Behr, A. Harrenga, A. Kannt, Annu. Rev. Biophys. Biomol. Struct. 27 (1998) 329.
[24] S. Hallen, T. Nilsson, Biochemistry 31 (1992) 11853.
[25] B.C. Hill, C. Greenwood, Biochem. J. 218 (1984) 913.
[26] R. van Eldik, T. Asano, W.J. le Noble, Chem. Rev. 89 (1989) 549.
[27] K. Hiromi, Kinetics of Fast Enzyme Reactions: Theory and Practice, Kodanshi Scientific Books, Kodanshi, Ltd., 1979.
[28] G.N. Lewis, M. Randall (Eds.), Thermodynamics, McGraw-Hill, Inc., NY, 1961.
[29] K.A. Connors (Ed.), Binding Constants, John Wiley and Sons, Inc., 1987.
[30] K.S. Peters, T. Watson, T. Logan, J. Am. Chem. Soc. 114 (1992) 4276.
[31] C. Di Primo, G.H.B. Hoa, E. Deprez, P. Douzou, S.G. Sligar, Biochemistry 32 (1993) 3671.
[32] J.A. Westrick, K.S. Peters, J.D. Ropp, S.G. Sligar, Biochemistry 29 (1990) 6741.
[33] P.J. Schulenberg, W. Gartner, S.E. Braslavsky, J. Phys. Chem. 99 (1995) 9617.
[34] A. Losi, I. Michler, W. Gartner, S.E. Braslavsky, Photochem. Photobiol. 72 (2000) 590.
[35] S.E. Braslavsky, G.E. Heibel, Chem. Rev. 92 (1992) 1381.
[36] K.S. Peters, T. Watson, K. Mar, Annu. Rev. Biophys. Biophys. Chem. 20 (1991) 343.
[37] D.E. Falvey, Photochem. Photobiol. 65 (1997) 4.
[38] R.W. Larsen, J. Osborne, T. Langley, R.B. Gennis, J. Am. Chem. Soc. 120 (1998) 8887.
[39] R.W. Larsen, Inorg. Chim. Acta 288 (1999) 74.
[40] R.W. Larsen, T. Langley, J. Am. Chem. Soc. 121 (1999) 4495.
[41] K.C. Hansen, R.S. Rock, R.W. Larsen, S.I. Chan, J. Am. Chem. Soc. 122 (2000) 11567.
[42] J. Miksovska, J. Day, R.W. Larsen, J. Biol. Inorg. Chem. 8 (2003) 621.
[43] J. Miksovska, R.W. Larsen, J. Prot. Chem. 22 (2003) 387.
[44] J. Miksovska, R.W. Larsen, Inorg. Chim. Acta 355C (2003) 116.
[45] R.P.-Y. Chen, J.J-T. Huang, H.-L. Chen, H. Jan, M. Velusamy, C.-T. Lee, W. Fann, R.W. Larsen, S.I. Chan, Proc. Natl. Acad. Sci. U.S.A. 101/19 (2004) 7305.
[46] J. Miksovska, R.W. Larsen, J. Inorg. Chem. 43 (2004) 4051.
[47] R.S. Rock, K.C. Hansen, R.W. Larsen, S.I. Chan, Chem. Phys. 307 (2004) 201.
[48] J. Miksovska, J. Norstrom, R.W. Larsen, J. Inorg. Chem. 44 (2005) 1006.
[49] J. Miksovska, C. Suquet, J.D. Satterlee, R.W. Larsen, Biochemistry 44 (2005) 10028.
[50] J. Miksovska, R.B. Gennis, R.W. Larsen, FEBS Lett. 579 (2005) 3014.
[51] J. Miksovska, R.B. Gennis, R.W. Larsen, Biochim. Biophys. Acta 1757 (2006) 182.
[52] N.N.-W. Kuo, J.J.-T. Huang, J. Miksovska, R.P.-Y. Chen, R.W. Larsen, S.I. Chan, J. Am. Chem. Soc. 127 (2005) 16945.
[53] C.K.N. Patel, A.C. Tam, Rev. Mod. Phys. 53 (1981) 517.
[54] W.B. Jackson, N.M. Amer, A.C. Boccara, D. Fournier, Appl. Optics 20 (1981) 1333.
[55] J.E. Rudzki, J.L. Goodman, K.S. Peters, J. Am. Chem. Soc. 107 (1985) 7849.
[56] L.J. Rothberg, J.D. Simon, M. Bernstein, K.S. Peters, J. Am. Chem. Soc. 105 (1983) 3464.
[57] J.H. Hannay, Eur. J. Phys. 4 (1983) 141.
[58] M. Momenteau, C.A. Reed, Chem. Rev. 94 (1994) 659.
[59] J.P. Collman, R. Boulatov, C.J. Sunderland, L. Fu, Chem. Rev. 104 (2004) 561.
[60] T.G. Traylor, Acc. Chem. Res. 14 (1981) 102.
[61] O.K. Medhi, S. Mazumdar, S. Mitra, Inorg. Chem. 28 (1989) 3243.
[62] J. Simplicio, Biochemistry 11 (1973) 2525.
[63] A.M. Jehanly, D.A. Stotter, M.T. Wilson, Eur. J. Biochem. 71 (1976) 613.
[64] Y. Huang, M.C. Marden, J.C. Lambry, M.-P. Fontaine-Aupart, R. Pansu, J.-L. Martin, C. Poyart, J. Am. Chem. Soc. 113 (1991) 9141.
[65] E.E. Scott, Q.H. Gibson, J.S. Olson, J. Biol. Chem. 276 (2001) 5177.
[66] R.R. Hung, J.J. Grabowski, J. Am. Chem. Soc. 114 (1992) 351.
[67] K. Hereman, in: R. van Eldik, J. Jonas (Eds.), High Pressure Chemistry and Biochemistry, Reidel Publishing Co., Dordrecht, Holland, 1987.
[68] B.A. Springer, S.G. Sligar, J.S. Olson, G.N. Phillips, Chem. Rev. 94 (1994) 699.
[69] M. Lim, T.A. Jackson, P.A. Anfinrud, J. Chem. Phys. 102 (1995) 4355.
[70] M. Lim, T.S. Jackson, P.A. Anfinrud, Science 269 (1995) 962.
[71] M.D. Chatfield, K.N. Walda, D. Magde, J. Am. Chem. Soc. 112 (1990) 4680.
[72] E.R. Henry, J.H. Sommer, J. Hofrichter, W. Eaton, J. Mol. Biol. 166 (1983) 443.
[73] F. Sato, Y. Shiro, Y. Sakaguchi, T. Iizuka, H. Kayashi, J. Biol. Chem. 265 (1990) 18823.
[74] V. Srajer, T. Teng, T. Ursby, C. Pradervand, Z. Ren, S. Adachi, W. Schildkamp, D. Bourgeois, M. Wulff, K. Moffat, Science 274 (1996) 1726.
[75] T.E. Carver, R.E. Brantley, E.W. Singleton, R.M. Arduini, M.L. Quilin, G.N. Philips, J.S. Olson, J. Biol. Chem. 267 (1992) 14443.
[76] T.G. Lambright, S. Balasubramanian, S.M. Decatur, S.G. Boxer, Biochemistry 33 (1994) 5518.
[77] E.E. Scott, Q.H. Gibson, J.S. Olson, J. Biol. Chem. 276 (2001) 5177.
[78] J.S. Oslon, G.N. Phillips, J. Biol. Chem. 271 (1996) 17593.
[79] M.F. Perutz, F.S. Mathews, J. Mol. Biol. 21 (1965) 199.
[80] D.A. Case, M. Karplus, J. Mol. Biol. 132 (1979) 343.
[81] J.A. Westrick, K.S. Peters, Biophys. Chem. 37 (1990) 73.
[82] J.A. Westrick, K.S. Peters, J.D. Ropp, S.G. Sligar, Biochemistry 29 (1990) 6741.
[83] K.S. Peters, T. Watson, K. Marr, Annu. Rev. Biophys. Biophys. Chem. 20 (1991) 343.
[84] L. Angeloni, A. Feis, Photochem. Photobiol. Sci. 2 (2003) 730.
[85] J.C. Moore, R.T. Battino, R. Rettich, Y.P. Handa, E. Wilhelm, J. Chem. Eng. Data 27 (1982) 22.
[86] T.V. Chalikian, Annu. Rev. Biophys. Biomol. Struct. 32 (2003) 207.
[87] G.S. Kachalova, A.N. Popov, H.D. Bartunik, Science 284 (1999) 473.
[88] S. Messa, E.J. Bedmar, A. Chanfon, H. Hennecke, H.M. Fischer, J. Bacteriol. 185 (2003) 3978.
[89] M.A. Sciotti, A. Chanfon, H. Hennecke, H.M. Fisher, J. Bacteriol. 185 (2003) 5639.
[90] M.A. Gilles-Gonzales, G. Gonzales, J. Inorg. Biochem. 99 (2005) 1.
[91] K.R. Rodgers, G.S. Lukat-Rodgers, J. Inorg. Biochem. (2005) 963.
[92] K.M. Chan, Curr. Opin. Chem. Biol. 5 (2001) 216.
[93] W. Gong, B. Hao, S.S. Mansy, G. Gonzalez, M.A. Gilles-Gonzalez, M.K. Chan, Proc. Natl. Acad. Sci. U.S.A. 95 (1998) 15177.
[94] W. Gong, B. Hao, M.K. Chan, Biochemistry 39 (2000) 3955.
[95] B. Hao, C. Isaza, J. Arndt, M. Soltis, M.K. Chan, Biochemistry 42 (2002) 12952.
[96] C.M. Dunham, E.M. Dioum, J.R. Tuckerman, G. Gonzalez, W.G. Scott, M.A. Gilles-Gonzales, Biochemistry 42 (2003) 7701.
[97] H. Miyatake, M. Mukai, S.-Y. Park, S.-I. Adachi, K. Tamura, H. Nakamura, K. Makamura, T. Tsuchiya, T. Iizuka, Y. Shiro, J. Mol. Biol. 301 (2000) 415.
[98] J. Key, K. Moffat, Biochemistry 44 (2005) 4627.
[99] J.R. Tuckermean, G. Gonzalez, E.M. Dioum, M.A. Gilles-Gonzales, Biochemistry (2002) 6170.

[100] K.R. Rogers, G.S. Lukat-Rogers, J.A. Barron, Biochemistry 35 (1996) 9539.
[101] S. Crosson, S. Rajagopal, K. Moffat, Biochemistry 42 (2003) 2.
[102] K.R. Rodgers, L. Tang, G.S. Lukat-Rodgers, N.L. Wengenack, Biochemistry 40 (2001) 12932.
[103] R.B. Gennis, Front. Biol. 9 (2004) 581.
[104] K. Faxen, G. Gilderson, P. Adelroth, P. Brzezinski, Nature 437 (2005) 286.
[105] S. Papa, Biochemistry (Moscow) 70 (2) (2005) 220.
[106] D. Bloch, I. Belevich, A. Jasaitis, C. Ribacka, A. Puustinen, M.I. Verkhovsky, M. Wikstrom, Proc. Natl. Acad. Sci. U.S.A. 101 (2004) 529.
[107] A. Namslauer, A.S. Pawate, R.B. Gennis, P. Brzezinski, Proc. Natl. Acad. Sci. U.S.A. 100 (2003) 15543.
[108] M. Wikstrom, A. Jasaitis, C. Backgren, A. Puustinen, M.I. Verkhovsky, Biochim. Biophys. Acta 1459 (2000) 514.
[109] A.A. Konstantinov, S. Siletsky, D. Mitchell, A. Kaulen, R.B. Gennis, Proc. Natl. Acad. Sci. U.S.A. 94 (1997) 9085.
[110] M. Olivberg, S. Hallen, T. Nilsson, Biochemistry 30 (1991) 436.
[111] D. Zaslavsky, A.D. Kaulen, I.A. Smirnova, T. Vygodina, A.A. Konstantinov, FEBS Lett. 336 (1993) 389.
[112] M.I. Verkhovsky, J.E. Morgan, M.L. Verkhovsky, M. Wikstrom, Biochim. Biophys. Acta 1318 (1997) 6.
[113] M. Karpefors, P. Adelroth, Y. Zhen, S. Ferguson-Miller, P. Brzezinski, Proc. Natl. Acad. Sci. U.S.A. 95 (1998) 13606.
[114] D.D. Lemon, M.W. Calhoun, R.B. Gennis, W.H. Woodruff, Biochemistry 32 (1993) 11953.
[115] O. Einarsdottir, B.R. Dyer, D.D. Lemon, P.M. Killough, S.M. Hubig, S.J. Atherton, J.J. Lopez-Garriga, G. Palmer, W.H. Woodruff, Biochemistry 32 (1993) 12013.
[116] D. Heitbrink, H. Sigurdson, C. Bolwien, P. Brzeninski, J. Heberle, Biophys. J. 82 (2002) 1.
[117] J.A. Bailey, F.L. Tomson, S.L. Mecklenburg, G.M. MacDonald, A. Katsonouri, A. Puustinen, R.B. Gennis, W.H. Woodruff, R.B. Dyer, Biochemistry 41 (2002) 2675.
[118] R.B. Gennis, FEBS Lett. 555 (2003) 2.
[119] E. Pinakoulaki, T. Soulimane, C. Varotsis, J. Biol. Chem. 277 (2002) 32867.
[120] D.M. Mitchell, J.D. Muller, R.B. Gennis, G.U. Nienhaus, Biochemistry 35 (1996) 16782.
[121] S. Stavrakis, K. Koutsoupakis, E. Pinakoulaki, A. Usbani, M. Saraste, C. Varatsis, J. Am. Chem. Soc. 124 (2002) 3814.
[122] D. Okuno, T. Iwase, K. Shinzawa-Itho, S. Yoshikawa, T. Kitagawa, J. Am. Chem. Soc. 125 (2003) 7209.
[123] D.T. Clark, A. Sgamellotti, F. Tarantelli, Inorg. Chem. 20 (1981) 2602.
[124] R.W. Larsen, Lett. FEBS 462 (1999) 75.
[125] M. Ralle, M.L. Verkhovskaya, J.E. Morgan, M.I. Verkovsky, M. Wikstron, N.J. Blackburn, Biochemistry 38 (1999) 7185.
[126] P. Adelroth, P. Brzezinski, B.G. Malmstron, Biochemistry 34 (1995) 2844.
[127] A. Namslauer, M. Branden, P. Brzezinski, Biochemistry 41 (2002) 10369.
[128] J.E. Morgan, P.M. Li, D. Jang, M.A. El-Sayed, S.I. Chan, Biochemistry 28 (1989) 6975.
[129] M.I. Verkhovsky, A. Jasaitis, M. Wikstrom, Biochim. Biophys. Acta 1506 (2001) 143.
[130] R.W. Larsen, Photochem. Photobiol. Sci. 5 (2006) 603.
[131] E. Pilet, A. Jasaitis, U. Liebel, M.H. Vos, Proc. Natl. Acad. Sci. U.S.A. 101 (2004) 16198.
[132] B.H. McMahon, M. Fabian, F. Tomson, T.P. Causgrove, J.A. Bailey, F.N. Rein, R.B. Dyer, G. Palmer, R.B. Gennis, W.H. Woodruff, Biochim. Biophys. Acta 1655 (2004) 321.
[133] P. Hellwig, B. Rost, W. Mantele, Spect. Chim. Acta A: Mol. Biomol. Spect. 57A (2001) 1123.
[134] D. Mauzerall, J.-M. Hou, V.A. Boichenko, Photosynth. Res. 74 (2002) 173.
[135] K. Ludmann, C. Gergely, G. Varo, Biophys. J. 75 (1998) 3110.
[136] A. Onufriev, A. Smondyrev, D. Bashford, J. Mol. Biol. 332 (2003) 1183.
[137] M.J.S. Dewar, K.M. Dieter, J. Am. Chem. Soc. 108 (1986) 8075.
[138] C. Ridley, J. Miksovska, A. Stern, T. Green, R. DeVane, B. Space, R.W. Larsen, Chem. Phys. Lett. 418 (2006) 137.
[139] G. Marriott, I. Parker (Eds.), Methods Enzymol, Vol. 360. Biophotonics (Part A), Academic Press, San Diego, 2003.
[140] S. Williams, T.P. Causgrove, R. Gilmanshin, K.S. Fang, R.H. Callender, W.H. Woodruff, R.B. Dyer, Biochemistry 35 (1996) 691.
[141] A.P. Williams, C.E. Longfellow, S.M. Freier, R. Kierzek, D.H. Turner, Biochemistry 28 (1989) 4283.
[142] T. Hara, N. Hirota, M. Terazima, J. Phys. Chem. 100 (1996) 10194.
[143] H. Chen, G.J. Diebold, J. Chem. Phys. 104 (1996) 6730.